Estimation of Nighttime Aerosol Optical Depths Using the Ground-based Microwave Radiometer

Guanyu Liu[1], Jing Li[1*], Sheng Yue[1], Lulu Zhang[1], Chongzhao Zhang[1]

[1] Department of Atmospheric and Oceanic Sciences, School of Physics, Peking University, Beijing, China

Corresponding authors: Jing Li (jing-li@pku.edu.cn)

Abstract

Aerosol optical depth (AOD) is a crucial parameter for understanding the impact of aerosols on Earth's atmosphere and air quality. Nevertheless, most existing remote sensing techniques rely on the shortwave spectrum, precluding nighttime measurements. While lunar and stellar photometry can measure nighttime AOD, their data availability is limited due to the scarce moonlight for lunar photometry and the rarity of application for stellar photometry. In this study, we made a first attempt to retrieve AOD from ground-based microwave radiometer (MWR) measurements in Beijing Nanjiao Meteorological Observatory in China. Brightness temperatures (BT) at the K band (from 22.23 GHz to 30.00 GHz) and V band (from 51.25 GHz to 58.80 GHz) are trained against daytime spectral AOD from sun-photometer measurements together with temperature profile using the random forest regression (RFR) retrieval model, and the model is then used to retrieve nighttime AOD. The algorithm demonstrates satisfactory performance, with reasonable agreements with lunar AOD retrievals from the lunar photometer (R=0.91 and RMSE=0.14). The results also reveal a distinct day-night cycle of AOD, with nighttime AOD typically higher than its daytime value for the Beijing-CAMS Aerosol Robotic Network (AERONET) site and AOD estimated based on MWR measurements. The physical basis of our approach is verified using vertical temperature and humidity profiles from sounding observation and simulation results from WRF-Chem as well as the MonoRTM. Our

删除[gyliu]: However,

删除[gyliu]: methods mostly

删除[gyliu]: which does not allow

删除[gyliu]: at nighttime

删除[gyliu]: .

删除[gyliu]: strong

删除[gyliu]: .

删除[gyliu]: .

study provides an effective and convenient approach to estimate nighttime aerosol loading from surface, which has great potential in environmental monitoring and climate forcing research.

1. Introduction

Aerosols have a significant impact on weather patterns and the Earth's climate (Huang et al., 2014; Li et al., 2022; Li et al., 2019; Riemer et al., 2019), offsetting about one-third of the warming effect by anthropogenic greenhouse gases and influence large-scale circulation (Huang et al., 2014; Li et al., 2022). However, accurately assessing their role in radiative forcing is a major challenge (Fan et al., 2016; Ghan et al., 2016; IPCC, 2021; Seinfeld et al., 2016). Monitoring aerosol optical depth (AOD) is crucial for understanding aerosol impacts on climate and air quality, as it reflects the total amount of aerosols in the atmosphere from its direct radiative impact (Visioni et al., 2023; Yang et al., 2020). As a result, there have been extensive efforts to measure AOD by various methods.

删除[gyliu]: optically

The AOD is firstly measured through the inversion of the Beer-Bouguer-Lambert law, which describes the attenuation of spectral direct normal irradiance (DNI) (Gueymard, 2012). This process typically involves the use of a spectrometer or spectroradiometer to measure direct solar irradiance as monochromatically as possible on a specific spectral channel (Gueymard, 2012). This can be achieved using either a filter-based photometer or a narrow-band spectroradiometer. The ground-based Cimel CE318-T sun photometer is widely used within the Aerosol Robotic Network (AERONET) to provide relatively accurate estimates of daytime AOD serving as referenced values since 1980s (Holben et al., 1998). Other observations measure physicochemical properties of aerosols instead of optical properties like AOD (Kremser et al., 2016; Li et al., 2016b). Mainstream aerosol remote sensing techniques rely on aerosol scattering of shortwave radiation in the ultraviolet and/or visible spectrum, thus only daytime AOD can be obtained (Sayer et al., 2019; Sun et al., 2021). However, aerosols typically have day-night variability, due to factors such as different emission sources, boundary layer structure, etc (Arola et al., 2013; Cachorro et al., 2004; Cachorro et al., 2008; Guo et al., 2017). Aerosols at nighttime also have detectable

删除[gyliu]: Remote sensing, either ground based or space borne, is an effective way to retrieve column AOD (Chaikovsky et al., 2020; Mhawish et al., 2017; Omar et al., 2013; Sinyuk et al., 2020).

impacts on the radiative balance, since they usually exert a warming effect in contrast to the cooling effect at daytime (Chen and Zhao, 2024; Colarco et al., 2014; Zhang et al., 2022), particularly in polar regions with the rapid change of AOD between daytime and nighttime (Chen and Zhao, 2024; Stenchikov et al., 2002; Wei et al., 2021). In special cases such as aerosols above the open oceans, they consistently exert a cooling influence in both shortwave and longwave, yet for dust aerosols, they potentially exert a warming effect in longwave during both day and night (Adebiyi et al., 2023; Feng et al., 2022; Song et al., 2022).

Remote sensing of aerosol properties at night is a challenging task. Lunar photometer emerges during recent years as an effective and relative accurate nighttime AOD retrieval technique, and has been widely used within the AERONET since 2013 (Barreto et al., 2013; Barreto et al., 2016). However, this method is limited in its temporal coverage, providing data for only approximately half of each month. This limitation arises because the method requires a substantial amount of moon-reflected solar radiation, which is not consistently available due to the imperfect anti-correlation between the lunar and solar set/rise cycles (Barreto et al., 2017; Berkoff et al., 2011). Compared with the lunar photometer method, stellar photometry, despite its rarity of use, provides nighttime AOD measurements by leveraging stellar irradiance, eliminating lunar phase corrections, with long-term datasets revealing diurnal aerosol dynamics (Pérez-Ramírez et al., 2011; Pérez-Ramírez et al., 2016; Pérez-Ramírez et al., 2008; Pérez-Ramírez et al., 2015). Arctic deployments and further development such as using a wide-field imager enhance its adaptability in extreme environments and spatiotemporal resolution, addressing gaps in traditional sun-photometer-based nocturnal monitoring (Ebr et al., 2021; Ivanescu et al., 2021; Ivanescu and O'Neill, 2023). However, this method is not widely adopted globally due to the bulkiness of the facilities and the complex operational processes required for deployment (Herber et al., 2002; LEITERER, 1995). Other researches take advantage of urban light to retrieve nighttime AOD from space from multiple sensors

删除[gyliu]: Aerosol Robotic Network (AERONET) (Barreto et al., 2016). However, this method can only provide data at ~ halftime each month since it requires a relatively large amount of moon-reflected solar radiation

删除[gyliu]: the star

删除[gyliu]: reliable

删除[gyliu]: O'neill

删除[gyliu]: .

(Jiang et al., 2022; Meng et al., 2023; Wang et al., 2023; Wang et al., 2020; Zhou et al., 2021). For example, Zhang et al. examined the effectiveness of retrieving nighttime AOD over urban areas by utilizing city lights observed through the satellite-based instrument VIIRS (Visible Infrared Imaging Radiometer Suite) Day-Night Band (DNB) (Zhang et al., 2019). However, this approach has limitations as it does not account for multiple scattering and gas absorption, which can potentially reduce the signals from aerosols (Zhou et al., 2021). Furthermore, these studies are constrained to the spatial scale of urban areas, resulting in vast rural regions being unexplored (Meng et al., 2023). Active remote sensing, such as lidars, can provide aerosol measurements at both day and night time (Balmes et al., 2021; Jiang et al., 2024). Nonetheless, solving the lidar equation requires assumption of the lidar ratio, and this assumed lidar ratio often causes large uncertainty of the retrieved extinction profiles as well as column integrated AOD usually (Liu et al., 2018; Rogers et al., 2014; Santa Maria and Winker, 2005). For the day-night difference of AOD, previous studies find slight increases of nighttime AOD using the long-term sun-and-star photometry data (Pérez-Ramírez et al., 2012; Pérez-Ramírez et al., 2016; Wang et al., 2004). Moreover, using Infrared Atmospheric Sounder Interferometer (IASI) and Cloud-Aerosol Transport System (CATS) are also effective methods to understand day-night differences in dust aerosols (Tindan et al., 2023; Yu et al., 2021). Grassl et al. (2024) also presented a homogenized dataset derived from a sun and star photometer operated in the European Arctic over a 20-year period. However, existing research regarding day-night difference of AOD only focuses on special types of aerosols such as dust aerosols, and has low availability due to the moon phase and urban light extent (Barreto et al., 2017; Jiang et al., 2022; Meng et al., 2023; Wang et al., 2023; Wang et al., 2020; Zhou et al., 2021). Due to our limited capability to measure nighttime AOD, there is a significant knowledge gap between daytime and nighttime aerosol properties.

In contrast to shortwave radiation which is only available during daytime, longwave radiation, especially in the thermal infrared and microwave spectrum, exists during both day and night, and offers the potential to derive nighttime aerosol property (Dufresne et al., 2002; Panicker et al., 2008). Previous research has explored the possibility to retrieve aerosol loading using longwave measurements, but mostly focused on large particles such as dust (Clarisse et al., 2019; DeSouza-Machado et al., 2010; Klüser et al., 2012; Pierangelo et al., 2004; Pierangelo et al., 2005; Zheng et al., 2022; Zheng et al., 2023). For example, using collocated thermal infrared observations from MODIS and dust optical depth from Cloud-Aerosol Lidar with Orthogonal Polarization (CALIOP), Zheng et al. simultaneously retrieve the thermal infrared dust optical depth and coarse-mode effective diameter over global oceans (Zheng et al., 2023). Observational and simulation studies indicate that the microwave brightness temperatures (BTs) and brightness temperature polarization differences may be both useful for estimating the dust mass loading (Ge et al., 2008; Hong et al., 2008; Huang et al., 2007; Mitra et al., 2013). Our previous study utilized satellite-based thermal infrared measurements in the atmospheric window region to retrieve nighttime AOD (Liu et al., 2024), and proves the effectiveness of these longwave measurements in deriving aerosol properties.

删除[gyliu]: Desouza

Ground-based microwave radiometer (MWR) is a widely used remote sensing instrument to retrieve temperature and humidity profiles using emitted longwave radiation by the surface-atmosphere system (Bianco et al., 2005; Greenwald et al., 2018; Knupp et al., 2009). Considering the aforementioned concepts of utilizing longwave radiances to retrieve aerosol properties and the potential alterations in microwave BTs due to the modified temperature and humidity profiles resulting from the shortwave radiation effect of aerosols, there is potential that aerosol information can be derived from MWR measurements, thereby further filling the gaps of previous retrieval methods. Therefore, in this study, we explore the possibility to retrieve AOD using surface based MWR measurements in the K spectral bands (22.23 GHz, 22.50

删除[gyliu]: .

GHz, 23.03 GHz, 23.83 GHz, 25.00 GHz, 26.23 GHz, 28.00 GHz, and 30.00 GHz) and V spectral bands (51.25 GHz, 51.76 GHz, 52.28 GHz, 52.80 GHz, 53.34 GHz, 53.85 GHz, 54.40 GHz, 54.94 GHz, 55.50 GHz, 56.02 GHz, 56.66 GHz, 57.29 GHz, 57.96 GHz, and 58.80 GHz). A machine learning based algorithm is developed to estimate AOD during both day and night. The theoretical basis of the method is further verified using regional model and radiative transfer simulations. The difference between day and night time AOD is also examined using the retrieval results.

2. Data and Methods

The retrieval algorithm used in this study is described in Figure 1 and includes four main steps: (1) preprocessing of input variables, (2) training the Random Forest Regression (RFR) retrieval model, (3) estimation of AOD using the trained model, and (4) independent validation to refine the model and assess its performance compared to lunar photometer observations. The details of the datasets and methods are explained below.

2.1 Datasets

The study area is located at the northern edge of the North China Plain, featuring a temperate continental monsoon climate with four distinct seasons (Yu et al., 2009). Spring is occasionally influenced by dust episodes transported by northwesterly and westerly winds from the Kumutage and Taklimakan deserts in western China, or by northerly winds from the Mongolian deserts (Liu et al., 2022a). Summer is marked by relatively hot and humid conditions and accounts for approximately 74% of the annual precipitation. Autumn is mild and dry, with clear skies and cooling temperatures. Winter is cold and dry, with occasional snowfall and minimal precipitation (Feng et al., 2010; Hao et al., 2017).

In this study, we utilized BT data collected from the MP-3000A MWR, which was stationed at the Beijing Nanjiao Meteorological Observatory located in China (39.80°N, 116.47°E, http://bj.cma.gov.cn/) (Ding et al., 2010; Lei et al., 2011; Zhou et al., 2024). The MP-3000A MWR is capable of detecting signals in the K-band (22 to 30 GHz) and V-band (51 to 59 GHz), and it is also equipped with additional features such as a precipitation sensor, an infrared radiation thermometer, and other relevant instruments. To maintain the accuracy and consistency of the atmospheric BT measurements, the MWR undergoes regular real-time calibration. These measurements are essential for obtaining temperature profiles and AOD data. Our analysis focuses on the K and V band of BT observations with 22 available channels, because BT observations at the K band are sensitive to water vapor absorption and BT observations at the V band are sensitive to oxygen absorption and temperature changes. We use the data ranging from December 2019 to October 2020 with a temporal resolution of one minute due to limitations of data distribution policy. We also aim to extend the temporal range of our analysis in the future study.

删除[gyliu]:).

The measured BTs include inaccuracies and unusual values caused by instrumental faults, calibration problems, and environmental factors. Hence, it's crucial to conduct quality control (QC) checks on the BT data before processing it further. These checks involve removing abnormal values to ensure that the BTs fall within a reasonable temperature range of 2.7 to 330 Kelvin, and inspecting for data consistency over time as per the methodology of Zhang et al. (Zhang, 2024). Ultimately, nearly 4.36% of BT data were excluded from the study due to a combination of instrumental faults, calibration problems, and environmental factors. Notably, the Level 2 sun photometer AOD products from AERONET are already validated and represent clear-sky conditions. Therefore, the collocation of MWR data with these AERONET products inherently excludes cloudy conditions. While AERONET data can be cloud-free in the direction of the sun, the MWR, which measures in the zenith direction, may still detect the presence of clouds. Therefore, we further conducted an additional cloud

删除[gyliu]: Notably, because the collocation between MWR and Level 2 sun photometer AOD products from the AERONET is already clear-sky data, there is no need to perform cloud screening on the MWR data.

screening following the method by the previous study to ensure the clear-sky conditions in the analysis (Zhang, 2024).

AOD retrieved using the solar and lunar methods at the Beijing-CAMS AERONET site (39.95°N,116.32°E, located in the Chinese Academy of Meteorological Sciences, see Table S1), which is the closest site to the MWR location (20.77 km), is used as training and validation data in the retrieval algorithm. For training our model, we utilized Level 2 sun photometer AOD products at the wavelengths of 440 nm, 500 nm, 675 nm, 870 nm, and 1020 nm during the day. Version 3 Level 1.5 lunar AOD products at the same wavelengths to validate AOD retrievals at night. It is noteworthy that the distance between the Beijing-CAMS AERONET site and MWR site is 20.77 km. Considering the vast urban area of Beijing, which spans approximately 160 km both east-west and north-south, this distance is relatively short. We specifically chose this AERONET station other than others because it is the only one that provides consistent Version 3 Level 1.5 lunar AOD products from 2019 to 2020, ensuring a consistent dataset with daytime AOD for our analysis.

删除[gyliu]: ,

删除[gyliu]: ,

删除[gyliu]: 440nm, 675nm, 870nm

删除[gyliu]: 1020nm

Given that MWRs are instrumental in tracking atmospheric temperature and humidity profile changes (Zhang et al., 2024), our method retrieves vertical temperature profiles concurrently. This is achieved by using temperatures at different pressure levels obtained from the European Center for Medium-Range Weather Forecasts (ECMWF) Reanalysis version 5 (ERA-5) as the target for our training (Hersbach, 2023). We chose the ECMWF products mainly because of their hourly temporal resolution, which provides more training samples for the RFR model than the twice-daily sounding data. This enhances the model's ability to capture temporal variability and improve prediction accuracy of the predicted variables. To further assess the accuracy of the model in predicting vertical temperature profiles, we utilized the collocated sounding data obtained from Beijing Meteorological Station (station ID: 54511) during the corresponding time frame. The collocation process

删除[gyliu]: .

involves identifying the temporally nearest valid BT measurement and subsequently inputting this BT value into the model to generate the MWR-based vertical temperature profile prediction. The radiosonde temperature profiles are then vertically interpolated to the standard pressure levels (100 hPa, 200 hPa, 500 hPa, 700 hPa, 850 hPa, and 1000 hPa) using a linear interpolation method, allowing for direct comparison with the MWR-based temperature profile prediction. These sounding data were collected twice daily respectively at 00:00 and 12:00 UTC from December 2019 to October 2020.

删除[gyliu]: 0000

删除[gyliu]: 1200

For the physical interpretation of our retrieval method, we employed collocated vertical profiles of temperature and relative humidity (RH) from the same sounding data under varying aerosol loadings to explore the effects of aerosol loading on the vertical profiles of meteorological variables. These vertical profiles were further utilized to compute BTs using the monochromatic radiative transfer model (MonoRTM).

In summary, our study primarily relies on in-situ measurements from three sites: the MWR site, the AERONET site, and the sounding site (see Table S1 and Figure 2b for details). These sites are located at the Beijing Nanjiao Meteorological Observatory, the Chinese Academy of Meteorological Sciences, and the Beijing Meteorological Station, respectively. All three sites are situated within the urban or suburban areas of Beijing, with relatively close proximity to each other. The aerosol types expected at these sites include urban aerosols and mixed aerosols, with dust aerosols peaking during the boreal spring season (Chen et al., 2016; Ou et al., 2017).

2.2 Retrieval Algorithm

Because the relationship between aerosol loading and microwave radiation is complicated and could be nonlinear, we use a machine learning based retrieval method focusing on the RFR method (Svetnik et al., 2003). The RFR model leverages

删除[gyliu]: All variables are appropriately matched in both space and time. Specifically, AOD from sun photometer measurements and BTs from the MWR are matched within a 5-minute time window, while hourly temperature profiles from ERA-5 reanalysis datasets and BTs from the MWR are collocated within a 30-minute time window and a 15 km spatial radius.

the power of ensemble learning, integrating multiple decision trees to enhance prediction accuracy and robustness. Each decision tree within the ensemble is constructed using a random subset of the training data and a random selection of features, thereby reducing overfitting and improving generalization capabilities. Through this mechanism, the RFR model can effectively capture the complex interactions between aerosol properties and microwave radiation signals, providing a reliable and efficient approach for aerosol retrieval.

All variables are rigorously matched in both temporal and spatial dimensions to ensure consistency and accuracy. Specifically, AOD data derived from sun photometer measurements are temporally matched with BTs from the MWR within a 5-minute time window. Meanwhile, hourly temperature profiles from the ERA-5 reanalysis datasets are collocated with MWR BTs within a 30-minute time window and a 15 km spatial radius. It should be noted that the acquisition of temperature profiles relies solely on the ERA-5 reanalysis data and does not require data from the AERONET station, and that the 15 km spatial radius only refers to the distance between the ERA-5 grid point and the MWR site location.

We first apply the relative importance feature selection technique, which is based on the Gini importance measure (Nembrini et al., 2018), to identify significant independent variables and build a generalized model. In the context of random forests, the relative importance of each predictor variable (feature) is quantified by a numeric array of size 1-by-Nvars. The importance measure for each variable is defined as the increase in prediction error that results from permuting the values of that variable across the out-of-bag observations. This measure is calculated for each tree in the ensemble, then averaged across all trees. To standardize the importance scores, the average values are normalized by dividing them by the standard deviation computed over the entire ensemble. This process yields a normalized importance measure that provides a robust assessment of each feature's contribution to the model's predictive

删除[gyliu]: The relative importance of each factor is presented in Figure 2.

performance. The relative importance of each factor is presented in Figure 3. It is observed that BTs across various frequency bands carry similar levels of importance, suggesting that the BTs are almost equally important for retrieving AOD.

The retrieval algorithm is subsequently trained using eight selected K-band BTs and fourteen V-band BTs from the MP-3000A MWR as input variables. The target variables include AOD at 440 nm, 500 nm, 675 nm, 870 nm, and 1020 nm from the Beijing-CAMS AERONET site, as well as ERA-5 vertical temperature profiles at 100 hPa, 200 hPa, 500 hPa, 700 hPa, 850 hPa, and 1000 hPa. To ensure the representativeness of the sampling, we select the first 3/4 of the data in each month as the training set and the last 1/4 of the data as the testing set. Additionally, the algorithm is adapted to estimate nighttime AOD using nighttime BTs from microwave radiometry as inputs, which is then validated against nighttime AOD observations from lunar measurements in lunar photometer for the same period. Moreover, AOD, whether in the visible or microwave region, is associated with aerosol loading, which serves as the foundation for retrieving visible AOD using microwave observations. Since we primarily aim at retrieving AOD rather than aerosol type, we did not consider AOD at the other wavelengths when building the AOD retrieval model. The relationship between AOD at 440 nm, 500 nm, 675 nm, 870 nm, and 1020 nm (the output wavelengths of the RFR model) and at the microwave band is enclosed in the random forest model. The model performance is assessed against photometer retrievals using metrics such as linear regression slope and intercept, correlation coefficient (R), root-mean-square error (RMSE), and mean absolute percentage error (MAPE).

The RFR model is built by varying the number of decision trees from 8 to 256. Through validation analysis, it is determined that the optimal number of trees is 128, based on the best performance during validation. The super parameters of this RFR model are detailed in Table S2. After refining the algorithm through extensive training

删除[gyliu]:

删除[gyliu]: Subsequently, the

删除[gyliu]: and

删除[gyliu]: , which

删除[gyliu]: sun photometer

删除[gyliu]: 440nm, 675nm, 870nm

删除[gyliu]: 1020nm

删除[gyliu]: 550nm

删除[gyliu]: that

and testing, it is used to retrieve nighttime AOD from nighttime MWR BTs, with validation against collocated lunar AOD measurements from the lunar photometer. Moreover, before investigating the diurnal cycle of MWR derived AOD, we perform a quality control on the minute-resolution retrieval results that typically have a higher noise level. Specifically, for each specific minute, we extract the AOD for this minute from each day to form an AOD sequence. We then calculate the mean and standard deviation of this AOD sequence. Finally, we remove AOD that exceeds three times the standard deviation. Considering the suitable quantity of outliers procured by setting the threshold at three standard deviations and the prevalently utilized 3-sigma rule, we used three standard deviations as the threshold (Li et al., 2016a; Liu et al., 2024; Wang et al., 2012).

2.3 WRF-Chem simulations

To investigate the effect of aerosols on downward microwave radiation, we use the Weather Research and Forecasting model with Chemistry (WRF-Chem) simulations combined with the MonoRTM radiative transfer model. Because MWR-observed BT change is not only due to AOD change but also reflects the change of meteorological conditions due to the AOD change, we apply WRF-Chem and MonoRTM radiation transfer model instead of radiative transfer simulations only.

WRF-Chem simulation runs from 00:00 UTC on 17 December 2016 to 00:00 UTC on 20 December 2016 (a 72-hour period). The simulation period is different from that of the retrieval because there are no updated emission fields for 2019 and 2020. The initial meteorological conditions used for the simulations are based on the National Center for Atmospheric Research (NCEP) Final Global Forecast System Operational Analysis (FNL) provided by the National Oceanic and Atmospheric Administration (NOAA), with a 1° × 1° spatial resolution and a 6-hour temporal interval. The emission fields used here are Emissions Database for Global Atmospheric Research (EDGAR), MIX, and Multi-resolution Emission Inventory for China (MEIC) (Crippa

删除[gyliu]: 0000

删除[gyliu]: 0000

et al., 2018; Li et al., 2017; Wang et al., 2014). The surface emissivity we used for simulation is the default data for WRF-Chem. The simulation domain encompasses the area of Beijing, Tianjin, and Hebei province (as shown in Figure 2a), with a center point at 40.00°N, 116.25°E. The model employs a three-tiered nesting configuration, featuring outer grids of 40 × 46 with a 90 km horizontal spacing, middle grids of 48 × 60 with a 30 km horizontal spacing, and inner grids of 51 × 72 with a 10 km horizontal spacing. The vertical atmosphere is segmented into 47 levels, ranging from the model's ground level to 100 hPa, encompassing both the surface and the upper atmosphere. Figure 3 illustrates the domains of the WRF model simulations and the location of the MWR deployed at the Beijing Nanjiao Meteorological Observatory in China. To further confirm our findings, we perform another set of parallel experiments lasting from 00:00 UTC on 3 December 2016 to 00:00 UTC on 5 December 2016 (a 48-hour period) with the same settings. Additionally, to augment the representativeness of our results, analogous WRF-Chem simulations were executed during the boreal summer from 00:00 UTC on 5 July 2016 to 00:00 UTC on 8 July 2016 (a 72-hour period). The choice of these simulation periods is based on the presence of significant pollution events, which provide a robust basis for examining the influence of aerosols on meteorological fields and the associated microwave BTs. The first day of both sets of experiments is used for model stabilization, and the subsequent days are utilized for analysis.

删除[gyliu]: 3

删除[gyliu]: 0000

删除[gyliu]: 0000

For the choices of physical parameterization schemes, we employ the Lin microphysics scheme, the rapid radiative transfer model for global climate model (GCM) applications (RRTMG) for shortwave radiation, the Yonsei University (YSU) boundary layer scheme, the Monin-Obukhov ground layer scheme, the Carbon-Bond Mechanism version Z (CBM-Z) for gas-phase chemistry, and the Model for Simulating Aerosol Interactions and Chemistry (MOSAIC). The model output has a one-hour temporal resolution. Here, we utilize AOD at 550 nm instead of 500 nm

because WRF-Chem does not simulate AOD at 500 nm. Thus, 550 nm was selected as the closest available alternative wavelength in the WRF-Chem output.

To investigate the responses of surface downward microwave radiation to aerosol loadings, we also conducted two parallel experiments with and without aerosol emissions in the study. Two simulations that are respectively, designated as "EXP_AER" and " EXP_NOAER" are carried out. The EXP_AER experiment is defined as a control simulation in which aerosol and aerosol precursor emission scheme is turned on. This aerosol emission includes emissions of carbon monoxide, nitrogen oxides, sulphate oxides, dust aerosols, biomass aerosols, biomass burning aerosols, sea salt aerosols and anthropogenic aerosols. The sensitivity experiment ("EXP_NOAER") is also conducted by closing corresponding aerosol and aerosol precursor emission scheme. The difference between control and sensitivity results are considered as the adjustments of vertical meteorological profiles to aerosol loadings. This method is also widely used to explore the radiative forcing of different kinds of aerosol and its effects on meteorological fields in previous studies (Chen et al., 2023c; Matsui et al., 2018).

删除[gyliu]: 2023

It is important to note that the aerosol-radiation interaction feature is activated in the WRF-Chem model to investigate the impact of aerosol loadings on meteorological fields. Subsequently, we input meteorological profile data from pollution cases without cloud cover at each grid point into the monochromatic radiative transfer model (MonoRTM) to calculate the corresponding BT responses at various frequencies within the K-band.

2.4 MonoRTM

The MonoRTM (Clough et al., 2005; Huang et al., 2013), developed by Atmospheric and Environmental Research (AER), is a radiative transfer model specifically

删除[gyliu]: ,

designed for microwave and millimeter-wave applications (Clough et al., 2005; Huang et al., 2013). This model is particularly useful in the microwave radiation calculation (Payne et al., 2011). In this study, it is used to calculate the brightness temperatures (BTs) associated with the simulated temperature and humidity vertical profiles from WRF-Chem.

删除[gyliu]: (Clough et al., 2005).

3. Results

3.1 Model fitting and validation

The AERONET AOD data are used for training and validating the model. Specifically, daytime AERONET AOD data are used for model training and testing. To ensure the representativeness of the sampling, we have partitioned the data such that the 3/4 of the data in each month are designated as the training set, while the remaining 1/4 serves as the testing set. After training, nighttime MWR BT measurements are input into the model to generate nighttime AOD estimates. These estimates are then compared with nighttime AERONET lunar AOD measurements for validation.

The retrieval model has great fitting performance, as shown by Figure 4. The model fitting reaches correlation coefficients of 0.98 for the 440 nm, 500 nm, 675 nm, 870 nm, and 1020 nm, respectively, albeit with a minor systematic low bias for high AOD scenarios, which is similar to MODIS AOD products (Levy et al., 2013). Due to the consistent model performance in all wavelengths (Figure 4), we will focus on results at 500 nm in the following discussions since this is typically the reference wavelength for satellite remote sensing (Levy et al., 2013).

删除[gyliu]: Due to the consistent model performance in all wavelengths (Figure 4), we will focus on results at 440 nm in the following discussions.

Figure 5 displays the comparison between the daytime and nighttime AOD independently retrieved by MWR using our algorithm and those from the sun and lunar photometer from December 2019 to October 2020. The model, tested during the daytime, utilized a dataset of over 3,000 samples and achieved correlation coefficients

of 0.96 for 500 nm (Figure 5a). The performance in 500 nm of the test set (R = 0.96, RMSE = 0.08, and MAPE = 0.11) is slightly inferior to the train set (R = 0.98, RMSE = 0.07, and MAPE = 0.10) regarding the statistical metrics (Figure 5a). Most points are concentrated on the 1:1 line, with RMSE within 0.08 and MAPE within 0.11. The accuracy of this estimation is similar to existing shortwave-based algorithms based on the satellite sensor such as the MODIS aerosol products (Levy et al., 2013). However, the key advantage of using microwave BT is the capability to retrieve AOD at night, a feature lacking in these shortwave-based algorithms (Figure 5b). Nighttime AOD retrieval reaches comparable performance to that for daytime, exhibiting a high correlation of 0.91 with lunar AOD. A minor systematic bias towards lower values in high AOD scenarios is also noted, with RMSE about 0.14 and MAPE approximately 0.27, indicating the overall satisfactory performance of MWR retrievals. In addition, the MWR results also well capture the spectral variation of AOD for fine (440 nm to 870 nm Angstrom index > 1) and coarse mode particles (440 nm to 870 nm Angstrom index < 1), as shown in Figure 6. Moreover, the MWR tends to underestimate AOD during both daytime and nighttime, particularly at shorter wavelengths. As the wavelength increases, this underestimation diminishes, and the MWR measurements align more closely with AERONET observations (Figure 6). This trend is observed for both fine-mode and coarse-mode aerosols (Figure 6).

For retrieving vertical temperatures profiles, similarly to the AOD, we also partitioned the data such that the 3/4 of the data in each month are designated as the training set, while the remaining 1/4 serves as the testing set. Our algorithm simultaneously retrieves daytime and nighttime temperature profiles. As shown in Figure 7 & Figure 8, atmospheric temperature retrieval results also demonstrate good performance and exceed those of AOD. This is expected since the main signals in the microwave come from emitted radiation by the atmosphere that is directly related to temperature. In detail, R is generally above 0.98 and all of the RMSEs are around 1.0 K in the training set (Figure 7). Similarly, the model's performance on the test set is somewhat lower

删除[gyliu]: 440

删除[gyliu]: 11

删除[gyliu]: 28

删除[gyliu]: for

compared to the training set, but remains satisfactory overall. Specifically, R is above 0.95 and all of the RMSEs are around 1.8 K the test set (Figure 8), comparable to previous studies using MWR to retrieval temperature profiles with an optimal estimation method (Cimini et al., 2006). The significant biases at some pressure levels may be attributed to the larger biases between sounding data and reanalysis data that is used to train the model (Varga and Breuer, 2022). Our model also well captures the characteristics of the climatological mean temperature vertical profile, with the error in each pressure layer within 1.5 K (Figure 9a). There exist greater RMSE and bias in low pressure levels partially due to the higher temperature variations in these levels, the overall RMSE and bias serve to illustrate the exemplary performance of the model in estimating the vertical temperature profiles (Figure 9b & c).

删除[gyliu]: data

In summary, the day and nighttime MWR-based AOD and vertical temperature profiles derived from our algorithm successfully capture the AOD variability and vertical temperature profile characteristics with satisfactory accuracy. This model also unveils the spectral characteristics of AOD, with higher wavelengths corresponding to lower AOD. With great performance through model validation, we will investigate the diurnal cycle of AOD in the following section.

3.2 The diurnal cycle of MWR derived AOD

We further examine the day-night differences in the AOD retrieved by MWR and compare them to those revealed by surface photometer. It should be noted that the analysis period in the following section remains from December 2019 to October 2020, contingent upon the availability of data. We acknowledge that the analysis period may not fully represent typical regional conditions due to COVID-19 (Lv et al., 2020; Sulaymon et al., 2021). However, the impact of COVID was mainly confined to January–March 2020. By April 2020, Beijing had largely recovered, with industrial and anthropogenic pollution sources returning to normal (Liu et al., 2022b; Tao et al., 2021).

Figure 10a-b illustrates the mean diurnal cycles of the photometer AOD and MWR-based AOD derived from BT observations at the Beijing Nanjiao Meteorological Observatory in China. Although the MWR-based AOD tends to underestimate extreme values relative to the photometer AOD, the MWR measurements exhibits strong agreement with the photometer AOD (Figure 10a-b). As shown in Figure 10a, mean diurnal AOD follows a bi-modal temporal distribution, with a greater peak ~21:00 and a secondary peak at ~03:00. The AOD stays relatively low from 06:00 to 10:00, gradually rises from 10:00 to 21:00, reaching the first peak at 21:00. After that greater peak, the AOD decreases from 22:00 to 00:00, and then increases again until it reaches the second peak at 03:00. This pattern is consistent across other spectral bands (675 nm, 870 nm, and 1020 nm, not shown here). This decrease may be attributed to the higher relative humidity near 23:00 and the corresponding aerosol scavenging effect, but further investigation is needed in future studies. Moreover, although the MWR-based AOD seems to underestimate the extreme pollutions with high AOD compared with photometer observation, since the number of upper outliers of AOD of the photometer is higher than that of MWR, the overall temporal pattern is similar to that of the photometer (Figure 10a).

The mean and median AOD values further support the above findings, highlighting higher nighttime AOD compared to daytime (Figure 10b). This difference is validated by the boxplots of MWR-based AOD and photometer AOD (Figure 10c), passing the Student's *t*-test significance test with $p \leqslant 0.05$. Specifically, the median daytime AOD is in the range of 0.15 to 0.28 for MWR and 0.15 to 0.27 for the photometer, while the median nighttime AOD is greater than 0.34 for MWR and higher than 0.30 for the photometer. Similarly, the mean daytime AOD is in the range of 0.25 to 0.35 for MWR and 0.24 to 0.32 for the photometer, while the mean nighttime AOD is greater than 0.40 for MWR and over 0.44 for the photometer. This discrepancy between daytime and nighttime AOD has also been observed in previous studies estimating nighttime AOD by incorporating infrared radiance measurement from the

删除[gyliu]: Because the number of nighttime AODs from the photometer is smaller than that during the daytime, but the number of nighttime AODs from the MWR is nearly equal to that during the daytime, this

删除[gyliu]: not

删除[gyliu]: entirely explained by the lack of data sampling

删除[gyliu]: needs

删除[gyliu]: the

删除[gyliu]: study

Atmospheric InfraRed Sounder (AIRS) instrument into the machine learning model, further corroborated by surface and space lidar measurements (Liu et al., 2024). Notably, the mean AOD tends to exceed the median AOD, partly due to the long-tail distribution of AOD and the presence of high extreme values (Sayer et al., 2019).

删除[gyliu]: Moreover, AOD at the other wavelengths (

We have further divided the results into four seasons and validated that the diurnal cycle of AOD is consistent across all seasons, with the most pronounced diurnal difference occurring in summer (Figure S1). It is noted that the lunar AOD is not available for JJA, which further underscores the supplementary role of MWR-predicted AOD in complementing lunar AOD measurements. The seasonal variation of AOD diurnal cycle agrees with previous studies derived from downscaling reanalysis datasets (Wang et al., 2025). The more significant diurnal difference in AOD during summer can be attributed to two primary factors. Firstly, the intense solar radiation and high temperatures prevalent in summer significantly promote the formation of aerosol particles through the process of gas-to-particle conversion (Chen et al., 2023a). Secondly, the high humidity levels in summer facilitate aerosol hygroscopic growth, which enhances aerosol extinction (Chen et al., 2023b; Lv et al., 2017). AOD at the other wavelengths (440 nm, 675 nm, 870 nm, and 1020 nm) exhibit similar diurnal patterns with peaks at about 20:00-22:00 (not shown here) and higher nighttime AOD in general (Figure 6).

The increase in nighttime AOD compared to daytime can be attributed to various factors, including a shallower mixed layer due to reduced horizontal mixing and transport, a decrease in atmospheric environmental capacity, higher relative humidity, enhanced aerosol hygroscopic growth, or intensified pollution emissions (Brock et al., 2016). Similar observations of elevated nighttime particle matter concentration have been reported in previous studies (Perrone et al., 2022; Su et al., 2023). However, research on nighttime aerosol properties is limited, warranting further analysis to fully understand these discrepancies, which exceeds the scope of this study.

In summary, by using the BT measured by the MWR to retrieve AOD during nighttime, we can uncover the daily cycle of AOD. This improves our understanding of the day-nighttime AOD variability, provides insights into the diurnal changes of atmospheric pollution and sheds light on nighttime aerosol radiative effects.

3.3 Physical interpretation

Since the machine learning technique does not necessarily represent the physical relationship between aerosol loading and microwave radiances, we further verify the theoretical basis of our technique by analyzing the observed temperature and RH profiles under various AOD levels and using WRF-Chem combined with MonoRTM simulations. The simulation is designed to establish a connection between aerosol loadings and microwave radiances. A set of sensitivity experiments with and without aerosol forcing is conducted using WRF-Chem as described in Section 2, whose atmospheric profiles, including temperature, water vapor, gases and aerosols, are then used as the inputs to the MonoRTM to simulate the downward microwave radiances (represented by BT) observed by the MWR. To mitigate the influence of surface temperature on BT, we maintained a consistent surface temperature range (265 K-270 K) throughout the simulation.

We first analyze the temperature and RH profiles from sounding observations under various AOD levels (Figure 11a-b & d-e). These AOD levels include light pollution (AOD<0.2), medium pollution (0.2<AOD<0.5), and heavy pollution (AOD>0.5) scenarios. The selection of this threshold is to ensure a balanced sample size for each scenario. All differences in the temperature and RH profiles under different AOD scenarios passed the significance test with $p \leqslant 0.1$ by the *t*-test. For the temperature profiles, a higher AOD corresponds to a lower temperature in the upper atmosphere, and vice versa (Figure 11a). However, for the low-level atmosphere, the temperature might first increase as AOD increases and then decrease with AOD as increases. This

is associated with aerosol type and optical properties (Che et al., 2024; Mahowald et al., 2011). For the RH vertical profiles, RH increases as AOD increases at all pressure levels (Figure 11b). This may be attributed to aerosol hygroscopic growth effect, leading to a higher AOD (Quan et al., 2018). Notably, since the collocation between MWR and Level 2 sun photometer AOD products from the AERONET is already clear-sky data, the vertical profiles of RH is relatively low. BTs at 22.23 GHz calculated by these vertical profiles from MonoRTM also demonstrate that BTs tend to increase with AOD (Figure 11c). BTs at other frequencies in the K band also show similar trend (not shown here). We have also conducted a detailed seasonal analysis and found similar responses in temperature, RH, and BT to AOD, with minor differences likely attributable to variations in aerosol types (Figure S2). Similarly, the WRF-Chem output also demonstrates the sensitiveness of temperature and RH vertical profiles to aerosol loading, contributing to statistically significant BT difference under different pollution levels (Figure 11d-f). Although there might be a significant discrepancy of BT between WRF simulation results and observations with regards to the range, the trend and overall pattern is quite similar, revealing the similar trends in BT as a function of AOD (Figure 11f). This suggests that despite the range discrepancies, the fundamental relationships between BT and AOD are consistent between observation and simulation. The above observational evidence might indicate that MWR estimate AOD by detecting the temperature and humidity profile differences caused by the presence of aerosols, but the impact of aerosols on microwave radiative transfer is highly complex, involving multiple processes such as aerosol scattering and absorption, changes in surface temperature and temperature/humidity profiles due to aerosol radiative and hygroscopic effects, and the nonlinear relationship between aerosol properties in the microwave and visible spectra. The above-mentioned complexities inspire us to conduct further simulation to verify the theoretical basis of our technique.

删除[gyliu]: indicates

删除[gyliu]: further verifying the theoretical basis of our technique.

Furthermore, to isolate the impact of AOD on BT, we have fixed the surface temperature between 270 K and 275 K in our analysis. The selection of this specific surface temperature range effectively minimizes the influence of temperature variability on BT. Our simulation results, illustrated in Figure 12 and 13, indicate that for all frequencies in the K band, BT increases as AOD levels increase. This phenomenon exists in both the daytime and nighttime. Specifically, at 22.23 GHz, BT levels for clean conditions range from 60 K to 80 K, while for polluted conditions they range from 80 to 130 K, showing a statistically significant difference at both daytime and nighttime (Figure 12a & 13a). BT levels at other frequencies support this trend, indicating that BT tends to increase with AOD (Figure 12b-d & 13b-d). The increase of K band BT with AOD might be related to coherent changes of water vapor and aerosols, either due to aerosol absorption of water or meteorological conditions that affect both water vapor and aerosols. When AOD is higher, RH is typically also higher, accompanied by more water vapor due to the hygroscopic growth effect of aerosols, as supported by previous analysis (Figure 11a & c). Since the K band includes the water vapor absorption line near 22.235 GHz, the BT in the K band is sensitive to water vapor, and thus the BT increases as AOD increases (Liu et al., 2014; Xie et al., 2013), further strengthening the theoretical foundation of the proposed approach.

In contrast to the observations in the K band, an analysis of the V band frequencies reveals a consistent decrease in BT with the reduction of AOD levels, applicable to both diurnal and nocturnal periods (Figure 12e-h & 13e-h), which well corresponds to the cooling effect of aerosols. Notably, at a frequency of 51.76 GHz, the BT levels exhibit a range of 264 K to 270 K under pristine atmospheric conditions, whereas under polluted conditions, these levels are observed to be between 262 K and 265 K. Although the magnitude of this change is less pronounced than that observed in the K band, it passes the statistical significance ($p \leqslant 0.1$ by the t-test), indicating a reliable and measurable effect. The detailed physical interpretation as follows: due to the

删除[gyliu]: Furthermore, our

删除[gyliu]: still

删除[gyliu]: The above-mentioned conclusion was further verified by simulations lasting from 0000 UTC on 3 December 2016 to 0000 UTC on 5 December 2016 (a 48-hour period) with the same settings (not shown).

presence of the oxygen absorption band within the frequency range of the V band, it is highly sensitive to changes in atmospheric temperature (Van Leeuwen et al., 2001). Variations in AOD can influence the atmospheric temperature profile as shown by observation and simulation (Figure 11b &d). Consequently, in cases when AOD is high, the BT in the V band decreases.

The above-mentioned conclusion was further verified by simulations lasting from 00:00 UTC on 3 December 2016 to 00:00 UTC on 5 December 2016 (a 48-hour period) with the same settings (not shown). In conclusion, MWR has the potential to estimate AOD by identifying the differences in temperature and humidity profiles, as well as the direct scattering and absorption signals that arise from varying aerosol loadings. While previous studies have demonstrated that large aerosol particles, particularly dust aerosols, can significantly influence microwave radiation and BT (Ge et al., 2008; Hong et al., 2008), the primary mechanism by which MWR estimates AOD in this study might be through detecting the changes of temperature and RH profiles.

To deepen our understanding of the impact of aerosol loading on longwave radiation, we conducted a comparative analysis using WRF-Chem. By comparing scenarios with aerosol loadings (EXP_AER) and without aerosol loadings (EXP_NOAER), we examined the differences in AOD, surface temperature (ST) and ground downward longwave radiation (GDLR). This comparison is specifically designed to examine the impact of aerosol loading on longwave radiation, particularly its spatial distribution. As such, no BT information is generated or output in this comparison experiment. The findings reveal that higher aerosol concentration levels have a negative effect on ST (Figure 14b & e), particularly during the daytime (Figure 14b), while positively influencing GDLR (Figure 14c & f), especially at nighttime (Figure 14f), which is consistent with the above MonoRTM calculations.

设置格式[gyliu]: 两端对齐，段落间距段前: 6 磅，段后: 23.4 磅

设置格式[gyliu]: 字体: 非倾斜，图案: 清除(白色)

The validity of the aforementioned conclusion was further corroborated through simulations that spanned from 00:00 UTC on 3 December 2016 to 00:00 UTC on 5 December 2016, encompassing a continuous 48-hour period, utilizing identical settings (not shown here). Additionally, to augment the representativeness of our results, analogous WRF-Chem simulations were executed during the boreal summer. Specifically, these simulations were conducted from 00:00 UTC on 5 July 2016 to 00:00 UTC on 8 July 2016, covering a 72-hour duration, and they also yielded consistent conclusions (Figure S3-S5).

4. Conclusions and Discussions

This study introduces a new method for estimating clear sky AOD using BT measurements in the K and V band obtained from the MWR. By establishing a strong correlation (R = 0.96, RMSE = 0.11, and MAPE = 0.11 in the daytime test set) between the photometer AOD and multiple BTs derived from the MWR at the Beijing Nanjiao Meteorological Observatory using a machine learning algorithm, we were able to accurately retrieve nighttime AOD (R = 0.91, RMSE = 0.14, and MAPE = 0.28) and vertical temperature profiles (R＞0.95 for all levels and RMSE＜2.20 K for all levels). This model also well captures the spectral characteristics of AOD with higher Angstrom index for fine-mode dominated AOD and lower Angstrom index for coarse-mode dominated AOD. After applying this model with satisfactory performance, we show that the AOD diurnal cycle and find that AOD values follow a bi-modal diurnal cycle temporal distribution, with a greater peak ~21:00 and a secondary peak at ~03:00, suggesting higher nighttime AOD compared with daytime. The difference between daytime and nighttime AOD observed in the MWR data well agrees with sun and lunar photometer observation as well as particle matter concentration observations.

删除[gyliu]: .

The theoretical basis of our algorithm is also confirmed by analyzing observational vertical profiles of temperature and RH under various AOD levels and WRF-Chem as

well as MonoRTM simulations. Observation indicated that the vertical profiles of temperature and RH have statistically significant differences ($p \leqslant 0.1$) under different AOD levels, suggesting that MWR might estimate AOD by detecting the temperature and humidity profile differences caused by various aerosol loadings. Simulation further indicated a consistent and mostly linear increase in BTs in the K band (increasing from ~70 K to ~105 K at 22.23 GHz) and decrease in BTs in the V band (decreasing from ~265 K to ~257 K at 51.76 GHz) with AOD (550 nm, the wavelength of WRF-Chem simulated AOD) across all time periods. Aerosols tend to induce a cooling effect at surface while increasing ground downward longwave radiation, especially at the nighttime. This study holds significant promise for environmental and climate research as MWR BT measurements can be obtained day and night without being hindered by bright surfaces. The methodology developed here can potentially be applied to MWRs in other locations worldwide to retrieve both daytime and nighttime AOD values. However, it is important to note that this investigation is preliminary and may contain uncertainties. It is also applicable under clear sky since during cloudy sky, the downward microwave radiation will be dominated by that emitted by clouds.

删除[gyliu]:

It is important to note that the analysis of AOD is specifically conducted for the Beijing Nanjiao Meteorological Observatory in China, covering the period from December 2019 to October 2020. This timeframe encompasses various climate and pollution conditions and is contingent upon the availability of data. Moving forward, we aim to extend the time range of our analysis and explore additional aerosol characteristics that may be inferred from BT measurements, such as aerosol absorption and layer height. This will enhance our understanding of aerosol distribution and properties, ultimately improving our ability to monitor and predict aerosol impacts on climate and the environment.

删除[gyliu]: Moving forward, we aim to

Code and data availability

The sun photometer AOD data was obtained from https://aeronet.gsfc.nasa.gov/new_web/webtool_aod_v3.html, last access: 20 Apr 2024; the lunar photometer AOD data was obtained from https://aeronet.gsfc.nasa.gov/new_web/webtool_aod_v3_lunar.html, last access: 20 Apr 2024; the temperature profile from the ERA-5 reanalysis data was downloaded from https://cds.climate.copernicus.eu/cdsapp#!/dataset/reanalysis-era5-pressure-levels?tab=overview, last access: 24 Apr 2024; the MonoRTM source code is available on https://github.com/AER-RC/monoRTM, last access 18 Apr 2024. The sounding data obtained from Beijing Meteorological Station (station ID: 54511) was obtained from https://weather.uwyo.edu/upperair/bufrraob.shtml.

Author contributions

GL and JL conceived the study and wrote the original draft. GL, SY, LZ, and CZ ran the simulation and conducted the corresponding analysis. All authors revised and reviewed the draft.

Competing interests

The authors declare that they have no known competing financial interests or personal relationships that could have appeared to influence the work reported in this paper.

Acknowledgments

The authors thank Pawan Gupta and Elena Lind for their effort in establishing and maintaining Beijing-CAMS AERONET site.

Financial support

This study is funded by the National Natural Science Foundation of China (NSFC) No. 42425503 and No. 42175144, and National Key Research and Development Program of China (grant no. 2023YFF0805401).

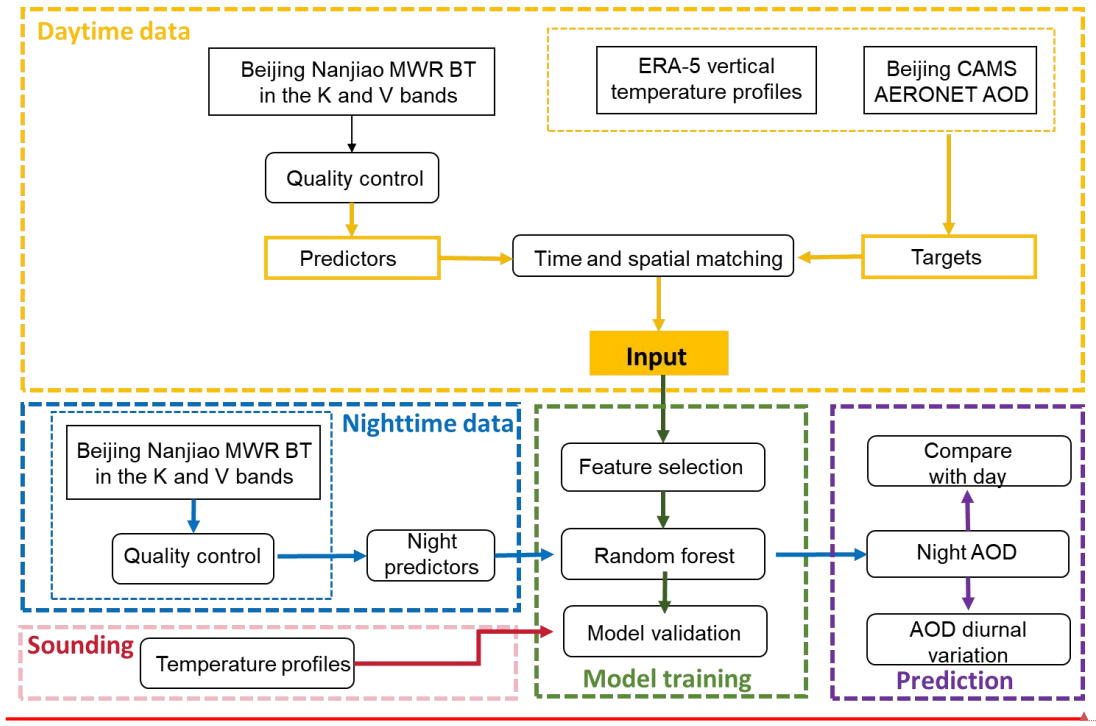

Figure 1. The flowchart for clear sky nighttime AOD and vertical temperature profiles retrieval algorithm.

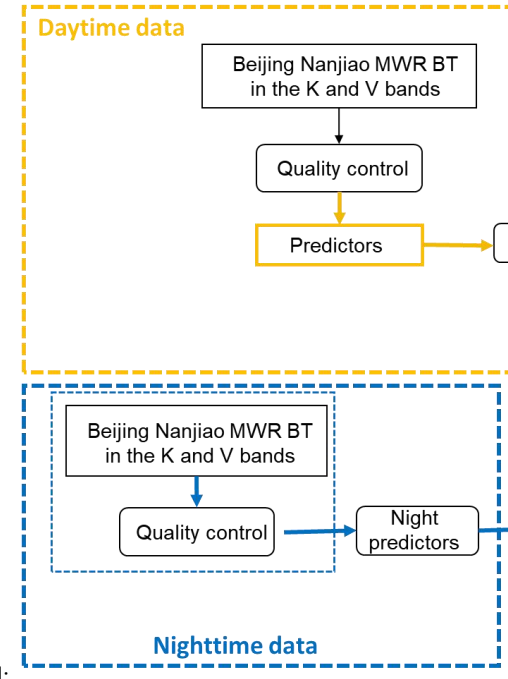

设置格式[gyliu]: 字体: 加粗

删除[gyliu]:

设置格式[gyliu]: 两端对齐

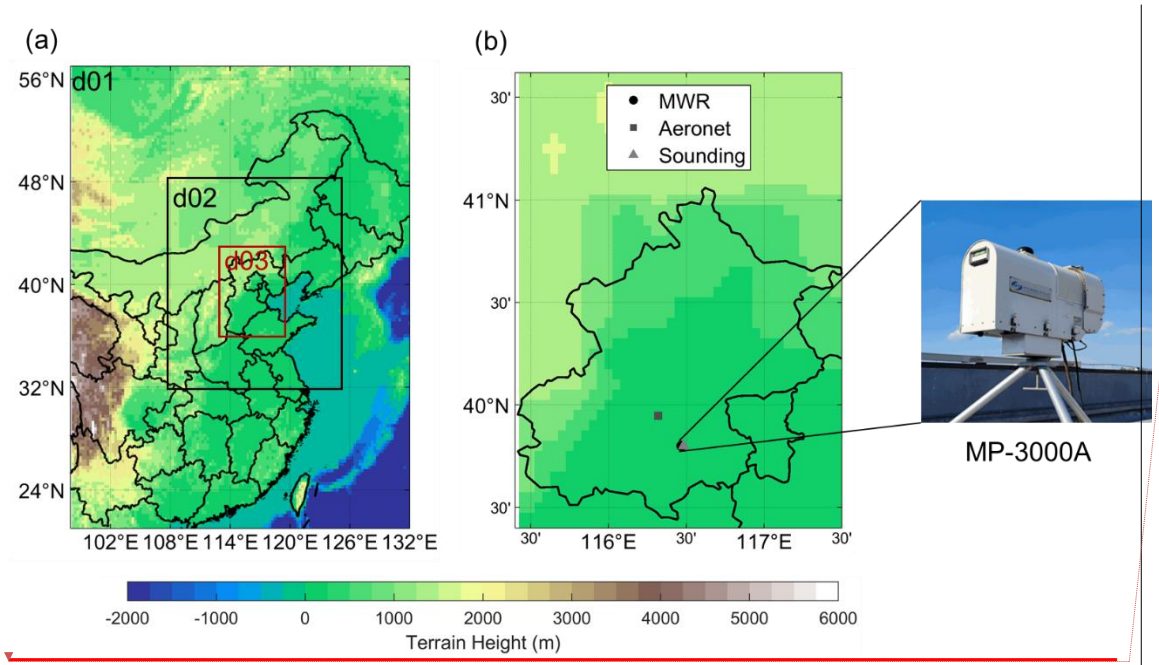

706

707 **Figure 2.** (a) Simulation domains of the WRF-Chem experiments. (b) Left panel: the
708 locations of observation sites in this study. The black circle indicates the MWR, the
709 dark grey square indicates the photometer, and the light triangle indicates the
710 sounding. Right panel: the MWR used in this study is located in domain 3. This
711 domain has a spatial resolution of 10 km. The MP-3000A MWR by Radiometrics is
712 deployed at the Beijing Nanjiao Meteorological Observatory (39.80°N, 116.47°E) in
713 China for brightness temperature (BT) measurements.

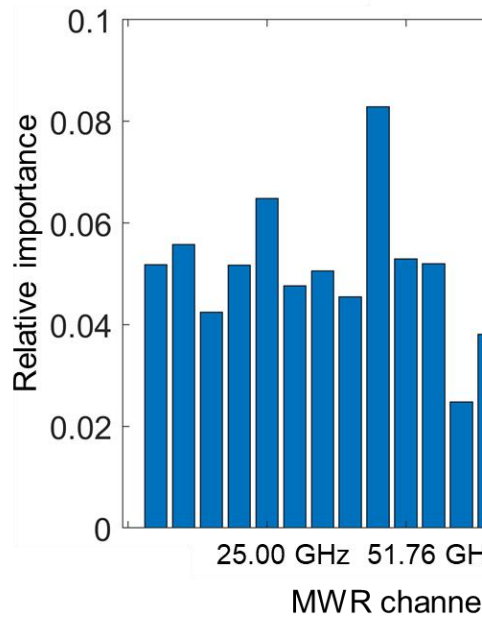

删除[gyliu]:
Figure 2.

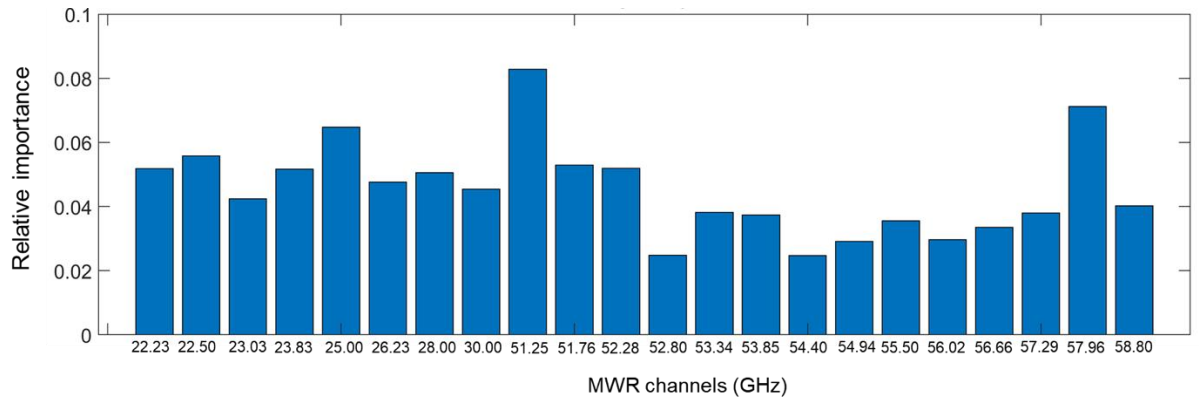

Figure 3. Relative importance of all BTs in different frequencies measured by MWR in the RFR model. The vertical axis represents relative importance (unitless), and the horizontal axis corresponds to different variable inputs (BTs in different frequencies measured by MWR in the RFR model). These channels include eight K bands (22.23 GHz, 22.50 GHz, 23.03 GHz, 23.83 GHz, 25.00 GHz, 26.23 GHz, 28.00 GHz, 30.00 GHz) and fourteen V bands (51.25 GHz, 51.76 GHz, 52.28 GHz, 52.80 GHz, 53.34 GHz, 53.85 GHz, 54.40 GHz, 54.94 GHz, 55.50 GHz, 56.02 GHz, 56.66 GHz, 57.29 GHz, 57.96 GHz, 58.80 GHz).

删除[gyliu]: band

删除[gyliu]: band

删除[gyliu]:

724

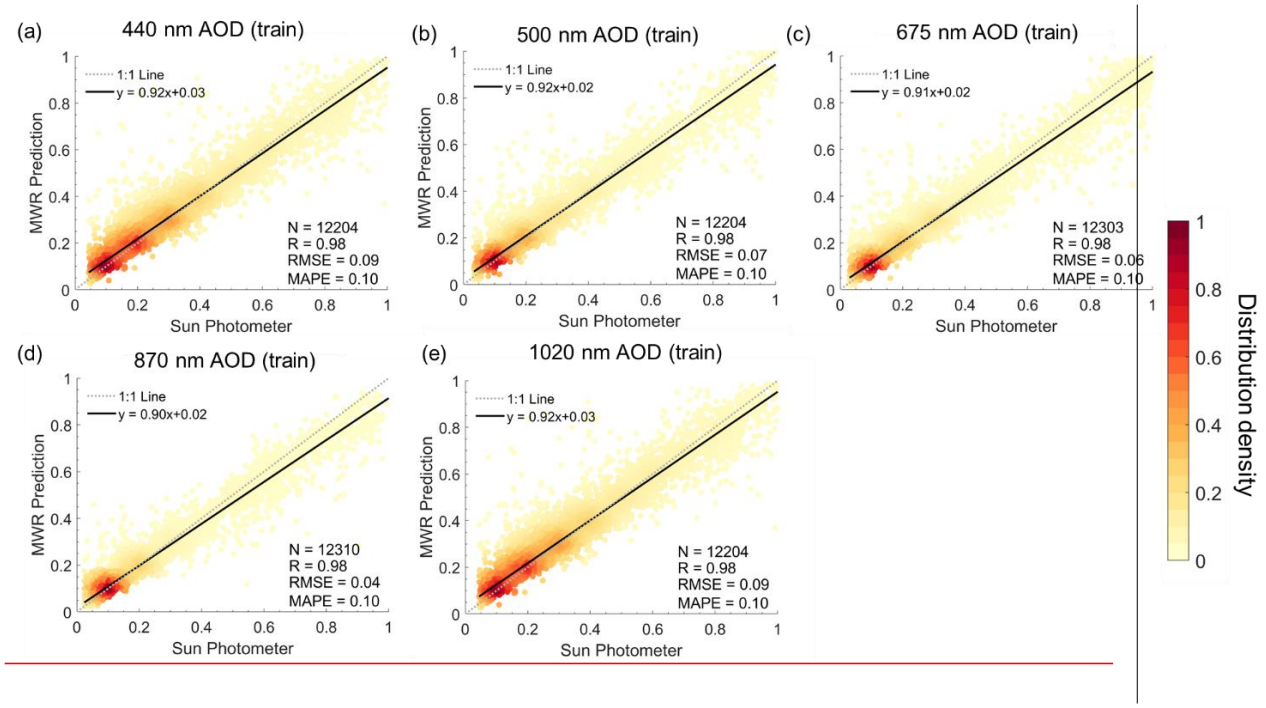

725 **Figure 4.** Density scatterplots of daytime AOD in the train set of MWR and sun
726 photometer with (a) 440 nm, (b) 500 nm, (c) 675 nm, (d) 870 nm, and (e) 1020 nm.
727 The dashed dark gray line represents the 1:1 line, and the black solid line represents
728 the linear regression line.

删除[gyliu]: c

删除[gyliu]: d

729

730

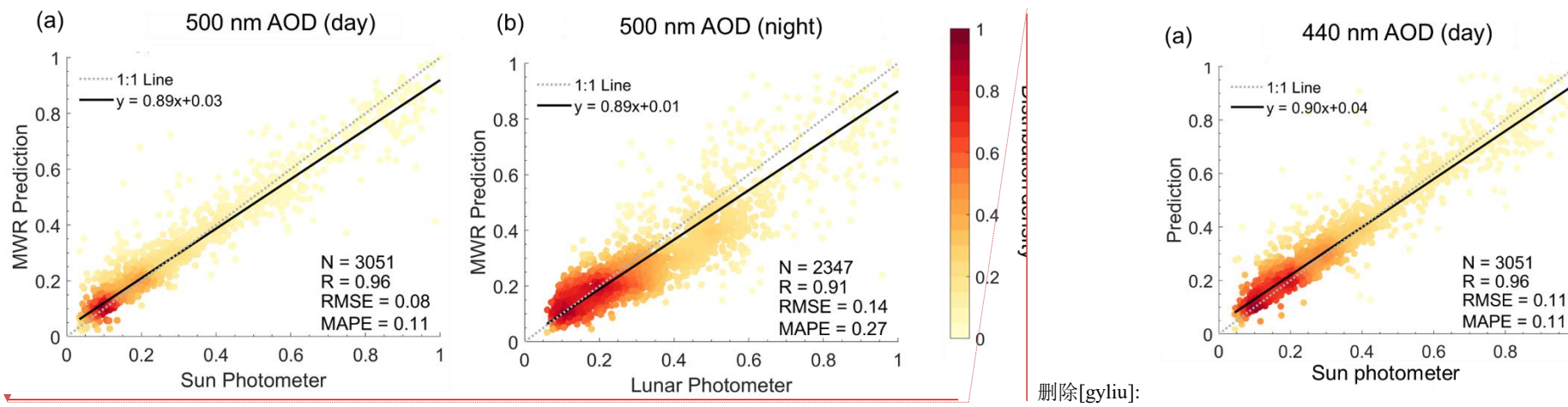

Figure 5. Density scatterplots of 500 nm AOD in the test set of MWR and the photometer with (a) daytime, and (b) nighttime. The dashed dark gray line represents the 1:1 line, and the black solid line represents the linear regression line. Note that the daytime corresponds to 6:00 am to 6:00 pm for the local time (UTC+8), and nighttime corresponds to the remaining time.

删除[gyliu]:

删除[gyliu]: 440

738

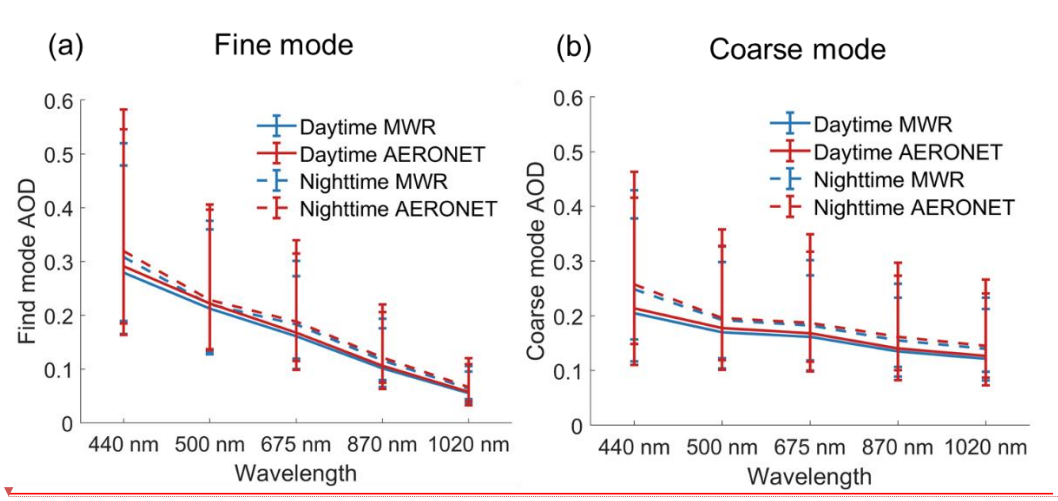

删除[gyliu]:

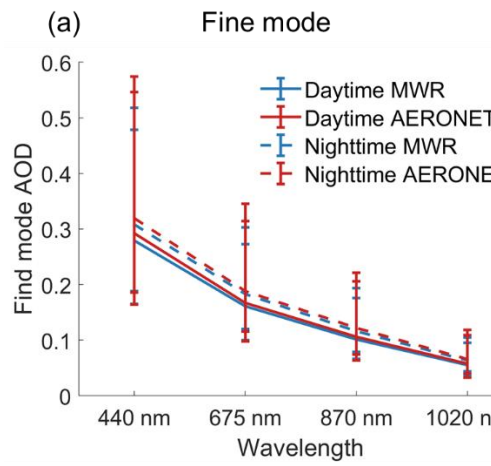

739 **Figure 6.** The relationship between wavelength and its corresponding AOD for
740 MWR-based (blue lines) and the photometer (red lines) in the daytime (solid lines)
741 and nighttime (dashed lines) for the (a) fine mode particles (440 nm to 870 nm
742 Angstrom index > 1), and (b) coarse mode particles (440 nm to 870 nm Angstrom
743 index < 1). The upper bound of the error bar is the 25th percentile, the middle is the
744 median, and the lower bound is the 75th percentile.

745

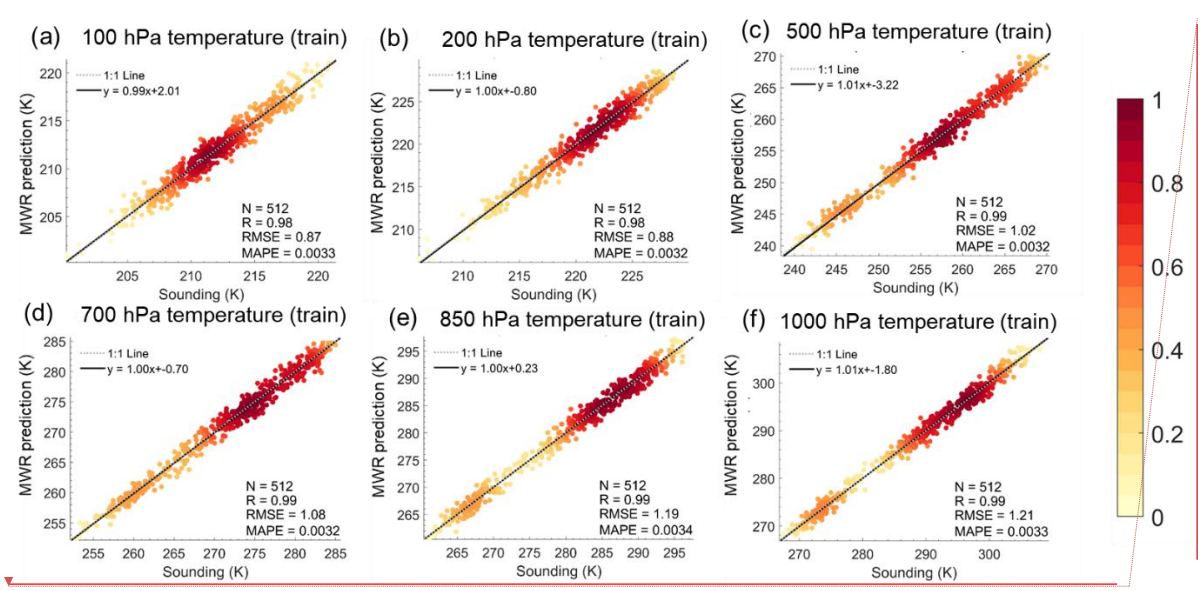

删除[gyliu]:

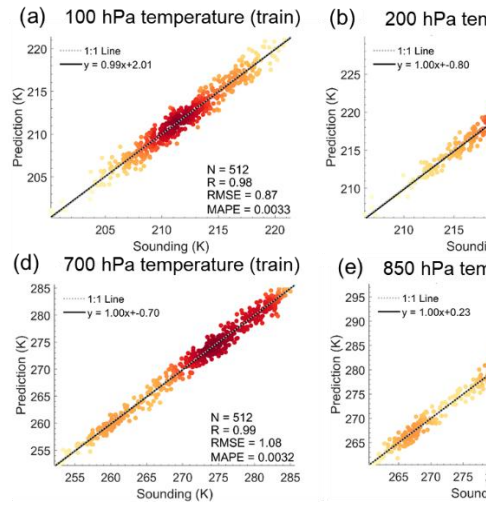

Figure 7. Density scatterplots of the vertical temperature profile in the train set of MWR and sounding data at (a) 100 hPa, (b) 200 hPa, (c) 500 hPa, (d) 700 hPa, (e) 850 hPa, and (f) 1000 hPa. The dashed dark gray line represents the 1:1 line, and the black solid line represents the linear regression line.

752 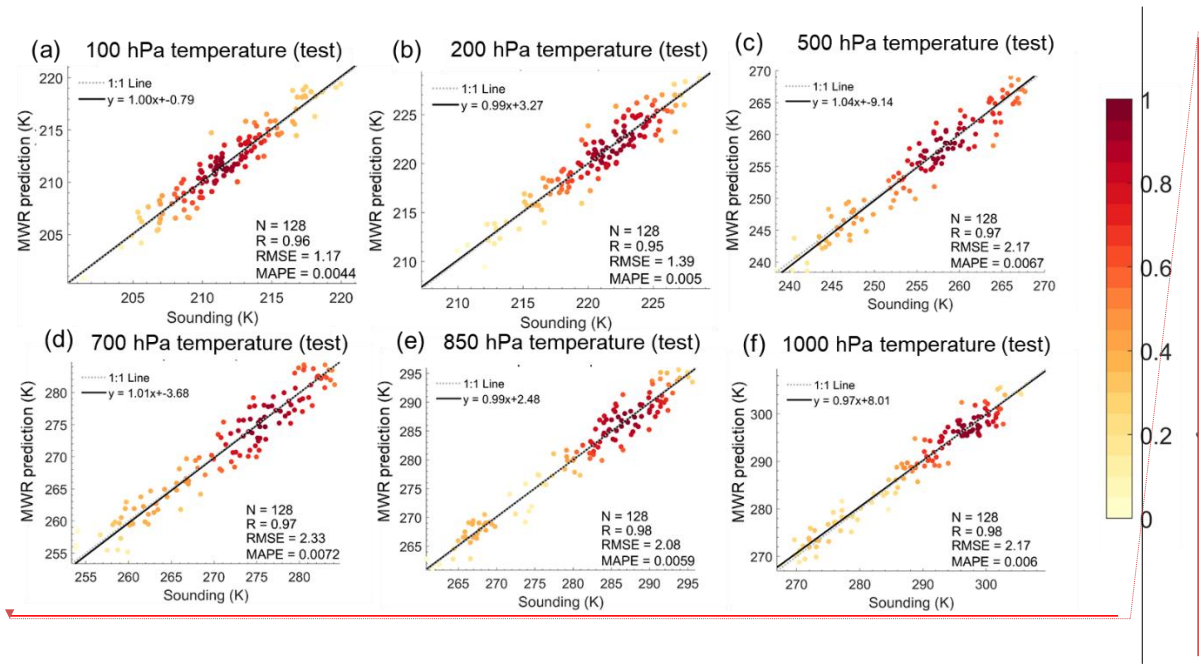

删除[gyliu]:

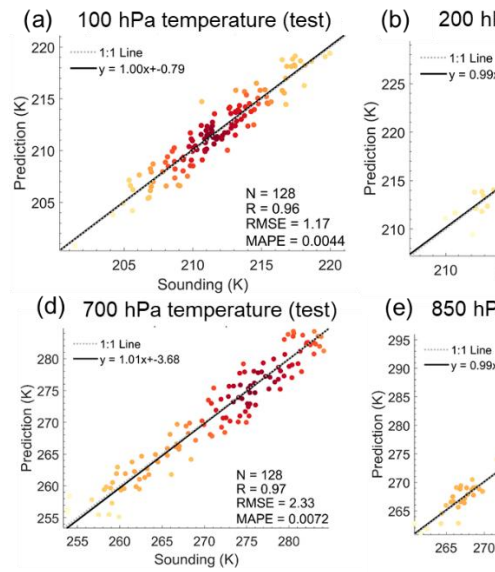

753 **Figure 8.** Density scatterplots of the vertical temperature profile in the test set of
754 MWR and sounding data at (a) 100 hPa, (b) 200 hPa, (c) 500 hPa, (d) 700 hPa, (e)
755 850 hPa, and (f) 1000 hPa. The dashed dark gray line represents the 1:1 line, and the
756 black solid line represents the linear regression line.

757

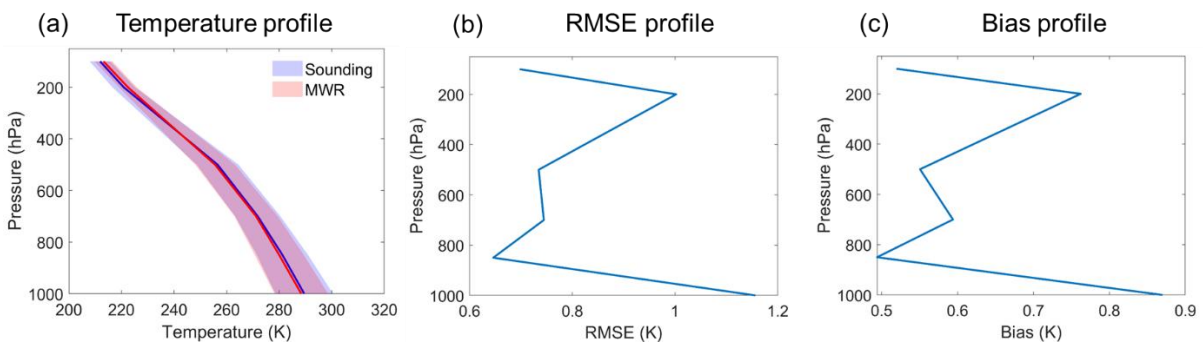

758

759 **Figure 9.** (a) Climatological mean vertical temperature profiles from sounding (the
760 blue shading and line) and MWR (the red shading and line). (b) RMSE vertical profile
761 calculated between sounding and MWR temperature, and (c) Similar to (b), but for the
762 bias vertical profile.

763

设置格式[gyliu]: 居中

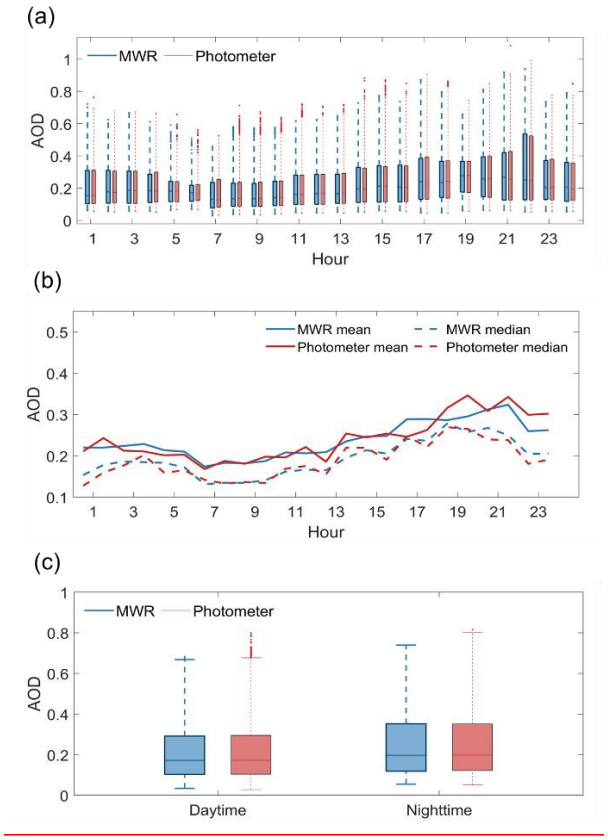

Figure 10. The diurnal cycle of annual mean MWR AOD and photometer AOD at 500 nm. (a) The boxplot of hourly MWR AOD (red boxplots) and photometer AOD (blue boxplots). The small dots represent outliers greater than $q_{75} + 1.5(q_{75} - q_{25})$ or less than $q_{25} - 1.5(q_{75} - q_{25})$, where q_{75} and q_{25} correspond to 75th and 25th percentile. (b) The time series of mean AOD (solid lines) and median AOD (dashed lines) of MWR AOD (red lines) and photometer AOD (blue lines). (c) The boxplot of daytime and nighttime AOD. Blue boxes correspond to MWR data, and red boxes correspond to photometer data.

删除[gyliu]:

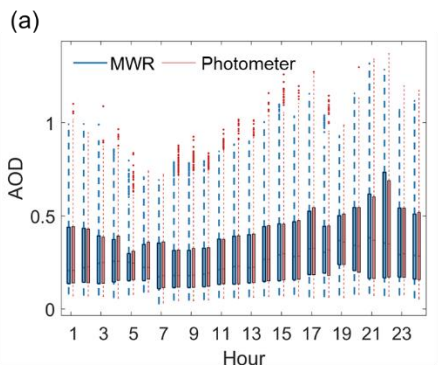

删除[gyliu]: 440nm

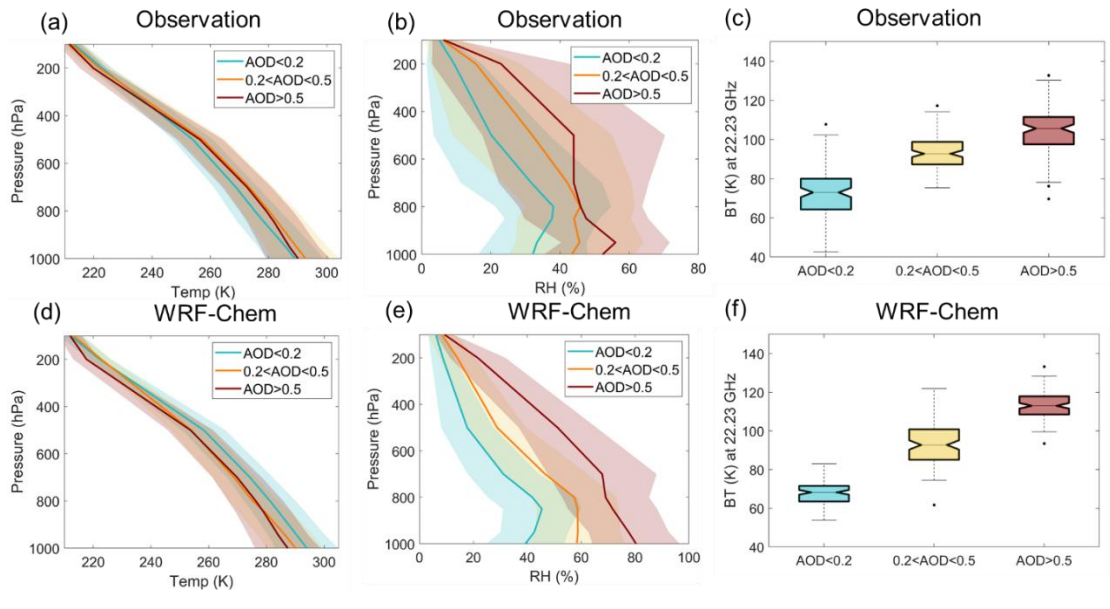

Figure 11. (a-b) The observational vertical profiles of temperature (Temp, unit: K) and relative humidity (RH, unit: %) under various AOD levels at 550 nm. The cyan, orange, and red solid lines correspond to low-level polluted scenarios (AOD<0.2), mid-level polluted scenarios (0.2<AOD<0.5), and high-level polluted scenarios (AOD>0.5). (c) Their corresponding brightness temperature (BT, unit: K) at 22.23 GHz calculated by MonoRTM. (d-f) Similar to a-c, but for the WRF-Chem simulation. The shadings represent the spread of samples with one standard deviation. All differences have passed the significance test of p-value≤0.01 by Student's t-test.

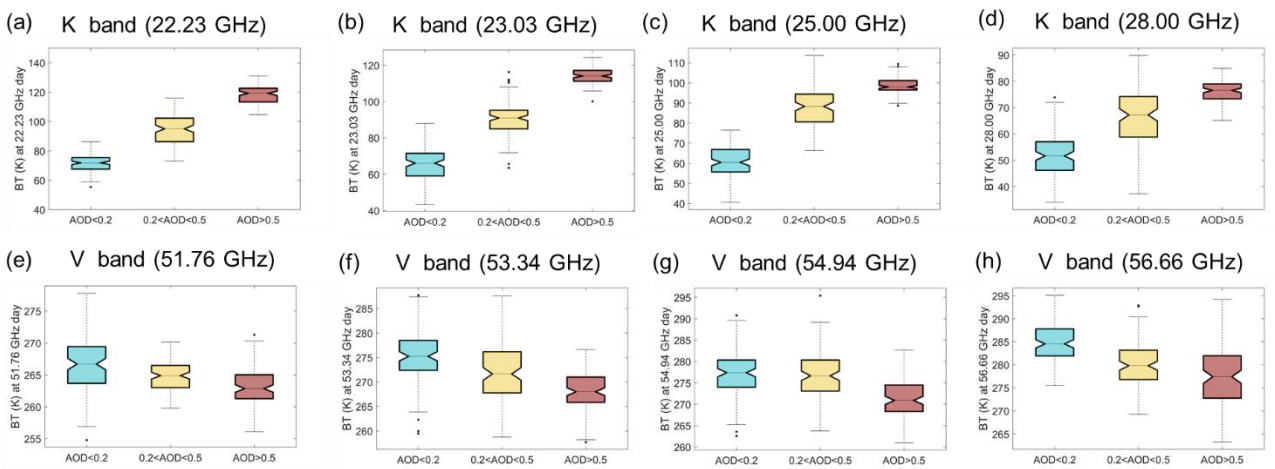

Figure 12. The boxplots of relationship between BT and AOD at 550 nm when fixing the surface temperature at 270-275 K from 00:00 UTC 18 December 2016 to 00:00 UTC 20 December 2016 in the WRF-Chem simulation. The frequencies of BT are (a) 22.23 GHz, (b) 23.03 GHz, (c) 25.00 GHz, (d) 28.00 GHz, (e) 51.76 GHz, (f) 53.34 GHz, (g) 54.94 GHz, and (h) 56.66 GHz during the daytime.

删除[gyliu]: 0000

删除[gyliu]: 0000

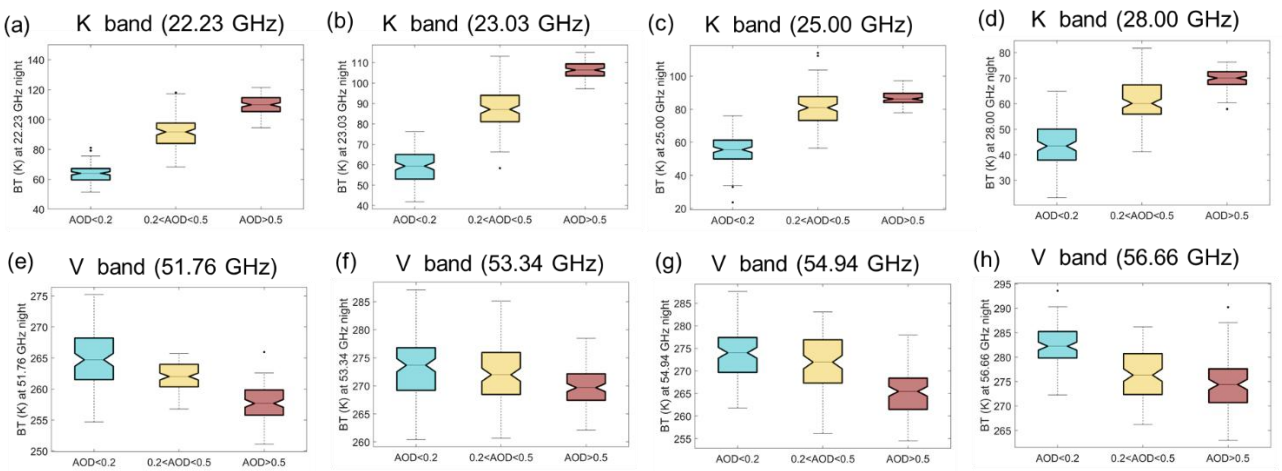

Figure 13. Similar to Figure 12, but for the nighttime.

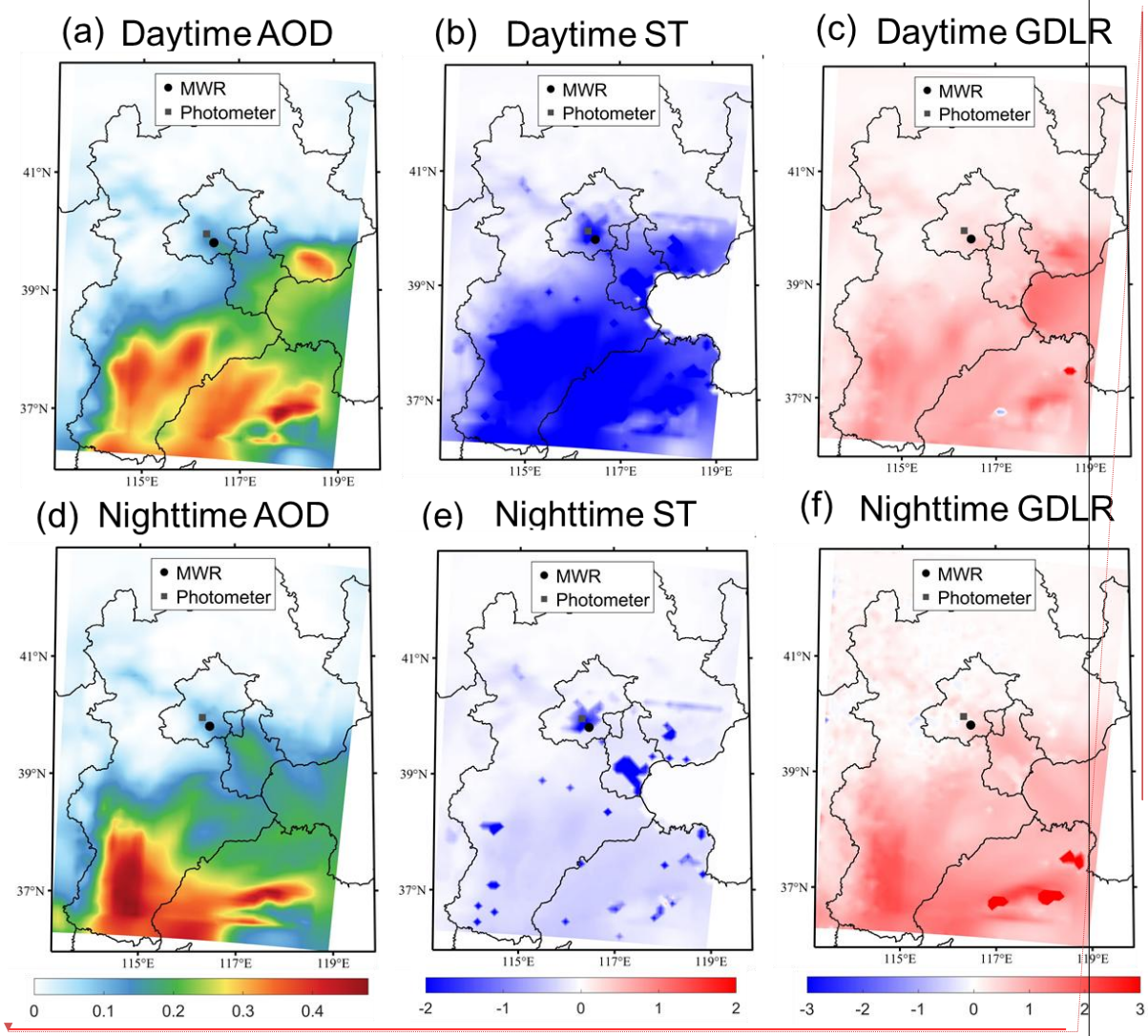

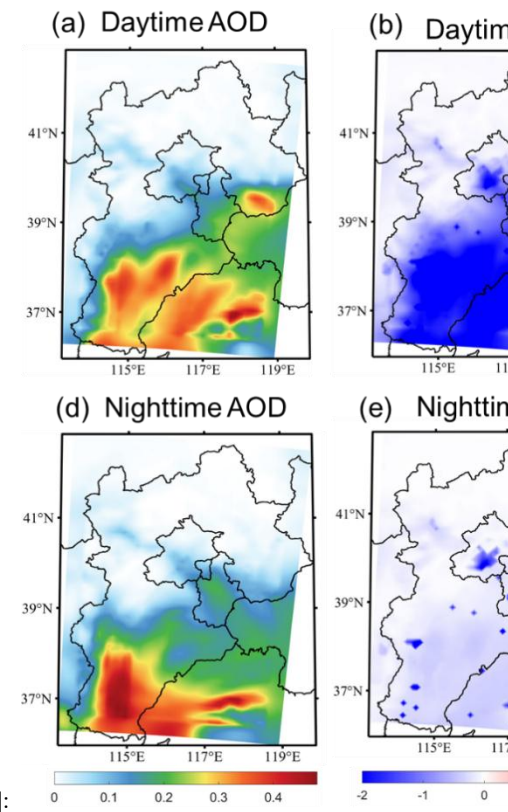

删除[gyliu]:

796

797 **Figure 14.** The difference of (a, d) aerosol optical depth (AOD, unitless), (b, e)
798 surface temperature (ST, K), and (c, f) ground downward longwave radiation (GDLR,
799 W/m^2) between EXP_AER and EXP_NOAER experiments
800 (EXP_AER-EXP_NOAER) during the (a-c) daytime and (d-f) nighttime. The black
801 circle indicates the MWR, and the dark grey square indicates the photometer. The
802 daytime corresponds to the period from 22:00 UTC 18 December 2016 to 10:00 UTC
803 19 December 2016. The nighttime corresponds to the period from 10:00 UTC 19
804 December 2016 to 22:00 UTC 19 December 2016.

删除[gyliu]: 2200

删除[gyliu]: 1000

删除[gyliu]: 1000

删除[gyliu]: 2200

805

References

设置格式[gyliu]: 英语(美国)

Adebiyi, A., Kok, J. F., Murray, B. J., Ryder, C. L., Stuut, J. B. W., Kahn, R. A., Knippertz, P., Formenti, P., Mahowald, N. M., Garcia-Pando, C. P., Klose, M., Ansmann, A., Samset, B. H., Ito, A., Balkanski, Y., Di Biagio, C., Romanias, M. N., Huang, Y., and Meng, J.: A review of coarse mineral dust in the Earth system, AEOLIAN RESEARCH, 60, 10.1016/j.aeolia.2022.100849, 2023.

Arola, A., Eck, T. F., Huttunen, J., Lehtinen, K. E. J., Lindfors, A. V., Myhre, G., Smirnov, A., Tripathi, S. N., and Yu, H.: Influence of observed diurnal cycles of aerosol optical depth on aerosol direct radiative effect, ATMOSPHERIC CHEMISTRY AND PHYSICS, 13, 7895-7901, 10.5194/acp-13-7895-2013, 2013.

Balmes, K. A., Fu, Q., and Thorsen, T. J.: The Diurnal Variation of the Aerosol Optical Depth at the ARM SGP Site, EARTH AND SPACE SCIENCE, 8, 10.1029/2021EA001852, 2021.

Barreto, A., Cuevas, E., Damiri, B., Guirado, C., Berkoff, T., Berjón, A. J., Hernández, Y., Almansa, F., and Gil, M.: A new method for nocturnal aerosol measurements with a lunar photometer prototype, ATMOSPHERIC MEASUREMENT TECHNIQUES, 6, 585-598, 10.5194/amt-6-585-2013, 2013.

Barreto, A., Roman, R., Cuevas, E., Berjon, A. J., Fernando Almansa, A., Toledano, C., Gonzalez, R., Hernandez, Y., Blarel, L., Goloub, P., Guirado, C., and Yela, M.: Assessment of nocturnal aerosol optical depth from lunar photometry at the Izana high mountain observatory, ATMOSPHERIC MEASUREMENT TECHNIQUES, 10, 3007-3019, 10.5194/amt-10-3007-2017, 2017.

Barreto, A., Cuevas, E., Granados-Munoz, M.-J., Alados-Arboledas, L., Romero, P. M., Groebner, J., Kouremeti, N., Almansa, A. F., Stone, T., Toledano, C., Roman, R., Sorokin, M., Holben, B., Canini, M., and Yela, M.: The new sun-sky-lunar Cimel CE318-T multiband photometer - a comprehensive performance evaluation, ATMOSPHERIC MEASUREMENT TECHNIQUES, 9, 631-654, 10.5194/amt-9-631-2016, 2016.

Berkoff, T. A., Sorokin, M., Stone, T., Eck, T. F., Hoff, R., Welton, E., and Holben, B.: Nocturnal Aerosol Optical Depth Measurements with a Small-Aperture Automated Photometer Using the Moon as a Light Source, JAtOT, 28, 1297-1306, 10.1175/JTECH-D-10-05036.1, 2011.

Bianco, L., Cimini, D., Marzano, F. S., and Ware, R.: Combining microwave radiometer and wind profiler radar measurements for high-resolution atmospheric humidity profiling, JAtOT, 22, 949-965, 10.1175/JTECH1771.1, 2005.

Brock, C. A., Wagner, N. L., Anderson, B. E., Beyersdorf, A., Campuzano-Jost, P., Day, D. A., Diskin, G. S., Gordon, T. D., Jimenez, J. L., Lack, D. A., Liao, J., Markovic, M. Z., Middlebrook, A. M., Perring, A. E., Richardson, M. S., Schwarz, J. P., Welti, A., Ziemba, L. D., and Murphy, D. M.: Aerosol optical properties in the southeastern United States in summer - Part 2: Sensitivity of aerosol optical depth to relative humidity and aerosol parameters, ATMOSPHERIC CHEMISTRY AND PHYSICS, 16, 5009-5019, 10.5194/acp-16-5009-2016, 2016.

Cachorro, V. E., Romero, P. M., Toledano, C., Cuevas, E., and de Frutos, A. M.: The fictitious diurnal cycle of aerosol optical depth: A new approach for "in situ" calibration and correction of AOD data series, GEOPHYSICAL RESEARCH LETTERS, 31, 10.1029/2004GL019651, 2004.

Cachorro, V. E., Toledano, C., Berjón, A., de Frutos, A. M., Torres, B., Sorribas, M., and Laulainen, N. S.: An "in situ" calibration correction procedure (KCICLO) based on AOD diurnal cycle:: Application to AERONET -: El Arenosillo (Spain) AOD data series, JOURNAL OF GEOPHYSICAL RESEARCH-ATMOSPHERES, 113, 10.1029/2007JD009673, 2008.

Che, H. Z., Xia, X. G., Zhao, H. J., Li, L., Gui, K., Zheng, Y., Song, J. J., Qi, B., Zhu, J., Miao, Y. C., Wang, Y. Q., Wang, Z. L., Wang, H., Dubovik, O., Holben, B., Chen, H. B., Shi, G. Y., and Zhang, X. Y.: Aerosol optical and radiative properties and their environmental effects in China: A review, EARTH-SCIENCE REVIEWS, 248, 10.1016/j.earscirev.2023.104634, 2024.

Chen, A., Yang, J., He, Y., Yuan, Q., Li, Z., and Zhu, L.: High spatiotemporal resolution estimation of AOD from Himawari-8 using an ensemble machine learning gap-filling method, SCIENCE OF THE TOTAL ENVIRONMENT, 857, 10.1016/j.scitotenv.2022.159673, 2023a.

Chen, A. N. and Zhao, C. F.: Progress of aerosol direct radiative forcing, CHINESE SCIENCE BULLETIN-CHINESE, 69, 30-44, 10.1360/TB-2023-0375, 2024.

Chen, H., Cheng, T., Gu, X., Li, Z., and Wu, Y.: Characteristics of aerosols over Beijing and Kanpur derived from the AERONET dataset, ATMOSPHERIC POLLUTION RESEARCH, 7, 162-169, 10.1016/j.apr.2015.08.008, 2016.

Chen, J., Shen, Y., Chi, X., and Zhu, S.: Factors influencing the hygroscopicity of aerosols and the effects of hygroscopicity on aerosol optical properties, Journal of Environmental Engineering Technology, 13, 2081-2091, 2023b.

Chen, Y., Chen, S. Y., Zhou, J., Zhao, D., Bi, H. R., Zhang, Y., Alam, K., Yu, H. P., Yang, Y. X., and Chen, J. Y.: A super dust storm enhanced by radiative feedback, NPJ CLIMATE AND ATMOSPHERIC SCIENCE, 6, 10.1038/s41612-023-00418-y, 2023c.

Cimini, D., Hewison, T. J., Martin, L., Güldner, J., Gaffard, C., and Marzano, F. S.: Temperature and humidity profile retrievals from ground-based microwave radiometers during TUC, MetZe, 15, 45-56, 10.1127/0941-2948/2006/0099, 2006.

Clarisse, L., Clerbaux, C., Franco, B., Hadji-Lazaro, J., Whitburn, S., Kopp, A. K., Hurtmans, D., and Coheur, P. F.: A Decadal Data Set of Global Atmospheric Dust Retrieved From IASI Satellite Measurements, JOURNAL OF GEOPHYSICAL RESEARCH-ATMOSPHERES, 124, 1618-1647, 10.1029/2018JD029701, 2019.

Clough, S. A., Shephard, M. W., Mlawer, E., Delamere, J. S., Iacono, M., Cady-Pereira, K., Boukabara, S., and Brown, P. D.: Atmospheric radiative transfer modeling: a summary of the AER codes, J. Quant. Spectros. Radiat. Transfer, 91, 233-244, 10.1016/j.jqsrt.2004.05.058, 2005.

Colarco, P. R., Nowottnick, E. P., Randles, C. A., Yi, B. Q., Yang, P., Kim, K. M., Smith, J. A., and Bardeen, C. G.: Impact of radiatively interactive dust aerosols in the NASA GEOS-5 climate model: Sensitivity to dust particle shape and refractive index, JOURNAL OF GEOPHYSICAL RESEARCH-ATMOSPHERES, 119, 753-786, 10.1002/2013JD020046, 2014.

Crippa, M., Guizzardi, D., Muntean, M., Schaaf, E., Dentener, F., van Aardenne, J. A., Monni, S., Doering, U., Olivier, J. G. J., Pagliari, V., and Janssens-Maenhout, G.: Gridded emissions of air pollutants for the period 1970-2012 within EDGAR v4.3.2, EARTH SYSTEM SCIENCE DATA, 10, 1987-2013, 10.5194/essd-10-1987-2018, 2018.

DeSouza-Machado, S. G., Strow, L. L., Imbiriba, B., McCann, K., Hoff, R. M., Hannon, S. E., Martins, J. V., Tanré, D., Deuzé, J. L., Ducos, F., and Torres, O.: Infrared retrievals of dust using AIRS: Comparisons of optical depths and heights derived for a North African dust storm to other collocated EOS A-Train and surface observations, JOURNAL OF GEOPHYSICAL RESEARCH-ATMOSPHERES, 115, 10.1029/2009JD012842, 2010.

Ding, H., Zheng, Z., and Liu, W.: Warming Trend and Seasonal Variation in Beijing During 1951-2008, Advances in Climate Change Research, 6, 187-191, 2010.

删除[gyliu]: Chaikovsky, A. P., Bril, A. I., Fedarenka, A. S., Peshcharankou, V. A., Denisov, S. V., Dick, V. P., Asipenka, F. P., Miatselskaya, N. S., Balin, Y. S., Kokhanenko, G. P., Penner, I. E., Samoilova, S. V., Klemasheva, M. G., Nasonov, S. V., Zhamsueva, G. S., Zayakhanov, A. S., Tsydypov, V. V., Batbold, A., Azzaya, D., Enkhbat, E., Oyunchimeg, D., Anh, N. X., Thanh, P. X., Hiep, N. V., Tuan, A. D., and Chen, B.: Synergy of Ground-Based and Satellite Optical Remote Measurements for Studying Atmospheric Aerosols, JApSp, 86, 1092-1099, 10.1007/s10812-020-00945-z, 2020.

删除[gyliu]: 2023

Dufresne, J. L., Gautier, C., Ricchiazzi, P., and Fouquart, Y.: Longwave scattering effects of mineral aerosols, JOURNAL OF THE ATMOSPHERIC SCIENCES, 59, 1959-1966, 10.1175/1520-0469(2002)059<1959:LSEOMA>2.0.CO;2, 2002.

Ebr, J., Karpov, S., Eliásek, J., Blazek, J., Cunniffe, R., Ebrová, I., Janecek, P., Jelínek, M., Jurysek, J., Mandát, D., Masek, M., Pech, M., Prouza, M., and Trávnícek, P.: A New Method for Aerosol Measurement Using Wide-field Photometry, ASTRONOMICAL JOURNAL, 162, 10.3847/1538-3881/abf7b1, 2021.

Fan, J. W., Wang, Y., Rosenfeld, D., and Liu, X. H.: Review of Aerosol-Cloud Interactions: Mechanisms, Significance, and Challenges, JOURNAL OF THE ATMOSPHERIC SCIENCES, 73, 4221-4252, 10.1175/JAS-D-16-0037.1, 2016.

Feng, T., Fu, Z.-T., and Mao, J.-Y.: The multi-fractal characteristics of climate variables in Beijing, CHINESE JOURNAL OF GEOPHYSICS-CHINESE EDITION, 53, 2037-2044, 10.3969/j.issn.0001-5733.2010.09.004, 2010.

Feng, Y., Wang, H., Rasch, P. J., Zhang, K., Lin, W., Tang, Q., Xie, S., Hamilton, D. S., Mahowald, N., and Yu, H.: Global Dust Cycle and Direct Radiative Effect in E3SM Version 1: Impact of Increasing Model Resolution, JOURNAL OF ADVANCES IN MODELING EARTH SYSTEMS, 14, 10.1029/2021MS002909, 2022.

Ge, J., Huang, J., Weng, F., and Sun, W.: Effects of dust storms on microwave radiation based on satellite observation and model simulation over the Taklamakan desert, ATMOSPHERIC CHEMISTRY AND PHYSICS, 8, 4903-4909, 10.5194/acp-8-4903-2008, 2008.

Ghan, S., Wang, M. H., Zhang, S. P., Ferrachat, S., Gettelman, A., Griesfeller, J., Kipling, Z., Lohmann, U., Morrison, H., Neubauer, D., Partridge, D. G., Stier, P., Takemura, T., Wang, H. L., and Zhang, K.: Challenges in constraining anthropogenic aerosol effects on cloud radiative forcing using present-day spatiotemporal variability, PROCEEDINGS OF THE NATIONAL ACADEMY OF SCIENCES OF THE UNITED STATES OF AMERICA, 113, 5804-5811, 10.1073/pnas.1514036113, 2016.

Greenwald, T. J., Bennartz, R., Lebsock, M., and Teixeira, J.: An Uncertainty Data Set for Passive Microwave Satellite Observations of Warm Cloud Liquid Water Path, JOURNAL OF GEOPHYSICAL RESEARCH-ATMOSPHERES, 123, 3668-3687, 10.1002/2017JD027638, 2018.

Gueymard, C. A.: Temporal variability in direct and global irradiance at various time scales as affected by aerosols, SoEn, 86, 3544-3553, 10.1016/j.solener.2012.01.013, 2012.

Guo, J. P., Xia, F., Zhang, Y., Liu, H., Li, J., Lou, M. Y., He, J., Yan, Y., Wang, F., Min, M., and Zhai, P. M.: Impact of diurnal variability and meteorological factors on the PM_{2.5} - AOD relationship: Implications for PM_{2.5} remote sensing, ENVIRONMENTAL POLLUTION, 221, 94-104, 10.1016/j.envpol.2016.11.043, 2017.

Hao, R., Wang, W., and Hao, J.: Classification of climate types and dynamic change in Beijing-Tianjin-Hebei region, Journal of Anhui Agricultural University, 44, 670-676, 2017.

Herber, A., Thomason, L. W., Gernandt, H., Leiterer, U., Nagel, D., Schulz, K. H., Kaptur, J., Albrecht, T., and Notholt, J.: Continuous day and night aerosol optical depth observations in the Arctic between 1991 and 1999, JOURNAL OF GEOPHYSICAL RESEARCH-ATMOSPHERES, 107, 10.1029/2001JD000536, 2002.

Hersbach, H., Bell, B., Berrisford, P., Biavati, G., Horányi, A., Muñoz Sabater, J., Nicolas, J., Peubey, C., Radu, R., Rozum, I., Schepers, D., Simmons, A., Soci, C., Dee, D., Thépaut, J-N: ERA5 hourly data on pressure levels from 1940 to present [dataset], 2023.

Holben, B. N., Eck, T. F., Slutsker, I., Tanre, D., Buis, J. P., Setzer, A., Vermote, E., Reagan, J. A., Kaufman, Y. J., Nakajima, T., Lavenu, F., Jankowiak, I., and Smirnov, A.: AERONET - A federated instrument network and data archive for aerosol characterization, REMOTE SENSING OF ENVIRONMENT, 66, 1-16, 10.1016/S0034-4257(98)00031-5, 1998.

Hong, G., Yang, P., Weng, F. Z., and Liu, Q. H.: Microwave scattering properties of sand particles: Application to the simulation of microwave radiances over sandstorms, J. Quant. Spectros. Radiat. Transfer, 109, 684-702, 10.1016/j.jqsrt.2007.08.018, 2008.

Huang, J. P., Ge, J. M., and Weng, F. Z.: Detection of Asia dust storms using multisensor satellite measurements, REMOTE SENSING OF ENVIRONMENT, 110, 186-191, 10.1016/j.rse.2007.02.022, 2007.

Huang, J. P., Wang, T. H., Wang, W. C., Li, Z. Q., and Yan, H. R.: Climate effects of dust aerosols over East Asian arid and semiarid regions, JOURNAL OF GEOPHYSICAL RESEARCH-ATMOSPHERES, 119, 11398-11416, 10.1002/2014JD021796, 2014.

Huang, X., Zhang, X., Leng, L., Li, F., and Fan, Y.: Study on retrieval methods with MonoRTM for microwave radiometer measurements, Scientia Meteorologlca Sinica, 33, 138-145, 2013.

IPCC: Short-Lived Climate Forcers. In Climate Change 2021: The Physical Science Basis. Contribution of Working Group I to the Sixth Assessment Report of the Intergovernmental Panel on Climate Change, Cambridge University Press, United Kingdom and New York, 10.1017/9781009157896.008, 2021.

Ivanescu, L. and O'Neill, N. T.: Multi-star calibration in starphotometry, ATMOSPHERIC MEASUREMENT TECHNIQUES, 16, 6111-6121, 10.5194/amt-16-6111-2023, 2023.

Ivanescu, L., Baibakov, K., O'Neill, N. T., Blanchet, J. P., and Schulz, K. H.: Accuracy in starphotometry, ATMOSPHERIC MEASUREMENT TECHNIQUES, 14, 6561-6599, 10.5194/amt-14-6561-2021, 2021.

Jiang, M., Chen, L., He, Y., Hu, X., Liu, M., and Zhang, P.: Nighttime aerosol optical depth retrievals from VIIRS day/night band data, National Remote Sensing Bulletin, 26, 493-504, 2022.

Jiang, X., Wang, Y., Wang, L., Tao, M., Wang, J., Zhou, M., Bai, X., and Gui, L.: Characteristics of Daytime-And-Nighttime AOD Differences Over China: A Perspective From CALIOP Satellite Observations and GEOS-Chem Model Simulations, JOURNAL OF GEOPHYSICAL RESEARCH-ATMOSPHERES, 129, 10.1029/2023JD039158, 2024.

Klüser, L., Kleiber, P., Holzer-Popp, T., and Grassian, V. H.: Desert dust observation from space - Application of measured mineral component infrared extinction spectra, ATMOSPHERIC ENVIRONMENT, 54, 419-427, 10.1016/j.atmosenv.2012.02.011, 2012.

Knupp, K. R., Ware, R., Cimini, D., Vandenberghe, F., Vivekanandan, J., Westwater, E., Coleman, T., and Phillips, D.: Ground-Based Passive Microwave Profiling during Dynamic Weather Conditions, JAtOT, 26, 1057-1073, 10.1175/2008JTECHA1150.1, 2009.

Kremser, S., Thomason, L. W., von Hobe, M., Hermann, M., Deshler, T., Timmreck, C., Toohey, M., Stenke, A., Schwarz, J. P., Weigel, R., Fueglistaler, S., Prata, F. J., Vernier, J. P., Schlager, H., Barnes, J. E., Antuña-Marrero, J. C., Fairlie, D., Palm, M., Mahieu, E., Notholt, J., Rex, M., Bingen, C., Vanhellemont, F., Bourassa, A., Plane, J. M. C., Klocke, D., Carn, S. A., Clarisse, L., Trickl, T., Neely, R., James, A. D., Rieger, L., Wilson, J. C., and Meland, B.: Stratospheric aerosol-Observations, processes, and impact on climate, REVIEWS OF GEOPHYSICS, 54, 278-335, 10.1002/2015RG000511, 2016.

977 Lei, L., Sun, J., and Wei, D.: Distinguishing the Category of the Summer Convective Weather by
978 Sounding Data in Beijing, Meteorological Monthly, 37, 136-141, 2011.
979 LEITERER, U., NAEBERT, A., NAEBERT, T., ALEKSEEVA, G.: A new star photometer developed
980 for spectral aerosol optical thickness measurements in Lindenberg, 1995.
981 Levy, R. C., Mattoo, S., Munchak, L. A., Remer, L. A., Sayer, A. M., Patadia, F., and Hsu, N. C.: The
982 Collection 6 MODIS aerosol products over land and ocean, ATMOSPHERIC MEASUREMENT
983 TECHNIQUES, 6, 2989-3034, 10.5194/amt-6-2989-2013, 2013.
984 Li, J., Li, C. C., Zhao, C. S., and Su, T. N.: Changes in surface aerosol extinction trends over China
985 during 1980-2013 inferred from quality-controlled visibility data, GEOPHYSICAL RESEARCH
986 LETTERS, 43, 8713-8719, 10.1002/2016GL070201, 2016a.
987 Li, J., Carlson, B. E., Yung, Y. L., Lv, D. R., Hansen, J., Penner, J. E., Liao, H., Ramaswamy, V., Kahn,
988 R. A., Zhang, P., Dubovik, O., Ding, A. J., Lacis, A. A., Zhang, L., and Dong, Y. M.: Scattering and
989 absorbing aerosols in the climate system, NATURE REVIEWS EARTH & ENVIRONMENT, 3,
990 363-379, 10.1038/s43017-022-00296-7, 2022.
991 Li, M., Zhang, Q., Kurokawa, J., Woo, J. H., He, K. B., Lu, Z. F., Ohara, T., Song, Y., Streets, D. G.,
992 Carmichael, G. R., Cheng, Y. F., Hong, C. P., Huo, H., Jiang, X. J., Kang, S. C., Liu, F., Su, H., and
993 Zheng, B.: MIX: a mosaic Asian anthropogenic emission inventory under the international
994 collaboration framework of the MICS-Asia and HTAP, ATMOSPHERIC CHEMISTRY AND
995 PHYSICS, 17, 935-963, 10.5194/acp-17-935-2017, 2017.
996 Li, W. J., Shao, L. Y., Zhang, D. Z., Ro, C. U., Hu, M., Bi, X. H., Geng, H., Matsuki, A., Niu, H. Y.,
997 and Chen, J. M.: A review of single aerosol particle studies in the atmosphere of East Asia:
998 morphology, mixing state, source, and heterogeneous reactions, JOURNAL OF CLEANER
999 PRODUCTION, 112, 1330-1349, 10.1016/j.jclepro.2015.04.050, 2016b.
1000 Li, Z. Q., Wang, Y., Guo, J. P., Zhao, C. F., Cribb, M., Dong, X. Q., Fan, J. W., Gong, D. Y., Huang, J.
1001 P., Jiang, M. J., Jiang, Y. Q., Lee, S. S., Li, H., Li, J. M., Liu, J. J., Qian, Y., Rosenfeld, D., Shan, S. Y.,
1002 Sun, Y. L., Wang, H. J., Xin, J. Y., Yan, X., Yang, X., Yang, X. Q., Zhang, F., and Zheng, Y. T.: East
1003 Asian Study of Tropospheric Aerosols and their Impact on Regional Clouds, Precipitation, and Climate
1004 (EAST-AIR_{CPC}), JOURNAL OF GEOPHYSICAL RESEARCH-ATMOSPHERES, 124,
1005 13026-13054, 10.1029/2019JD030758, 2019.
1006 Liu, C. S., Shen, X. X., and Gao, W.: Intercomparison of CALIOP, MODIS, and AERONET aerosol
1007 optical depth over China during the past decade, IJRS, 39, 7251-7275,
1008 10.1080/01431161.2018.1466070, 2018.
1009 Liu, D. W., Lv, C. C., Liu, K., Xie, Y., and Miao, J. G.: Retrieval Analysis of Atmospheric Water
1010 Vapor for K-Band Ground-Based Hyperspectral Microwave Radiometer, IEEE GEOSCIENCE AND
1011 REMOTE SENSING LETTERS, 11, 1835-1839, 10.1109/LGRS.2014.2311833, 2014.
1012 Liu, G. Y., Li, J., Jiang, Z. J., and Li, X. C.: Impact of sea surface temperature variability at different
1013 ocean basins on dust activities in the Gobi Desert and north China, Geophysical Research Letters, 49,
1014 e2022GL099821, 10.1029/2022GL099821, 2022a.
1015 Liu, G. Y., Li, J., Li, J., Yue, S., and Zhou, R. L.: Estimation of Nighttime Aerosol Optical Depths
1016 Using Atmospheric Infrared Sounder Longwave Radiances, GEOPHYSICAL RESEARCH LETTERS,
1017 51, 10.1029/2023GL108120, 2024.
1018 Liu, S., Yang, X. C., Duan, F. Z., and Zhao, W. J.: Changes in Air Quality and Drivers for the Heavy
1019 PM2.5 Pollution on the North China Plain Pre- to Post-COVID-19, INTERNATIONAL JOURNAL OF
1020 ENVIRONMENTAL RESEARCH AND PUBLIC HEALTH, 19, 10.3390/ijerph191912904, 2022b.

删除[gyliu]: G.

删除[gyliu]: Li, J., Li, J., Yue, S.,

删除[gyliu]: Zhou, R. L.: Estimation

删除[gyliu]: Nighttime Aerosol Optical Depths Using

删除[gyliu]: Infrared Sounder Longwave Radiances, GEOPHYSICAL RESEARCH

删除[gyliu]: 51

删除[gyliu]: 1029/2023GL108120, 2024

Lv, M., Liu, D., Li, Z., Mao, J., Sun, Y., Wang, Z., Wang, Y., and Xie, C.: Hygroscopic growth of atmospheric aerosol particles based on lidar, radiosonde, and in situ measurements: Case studies from the Xinzhou field campaign, J. Quant. Spectros. Radiat. Transfer, 188, 60-70, 10.1016/j.jqsrt.2015.12.029, 2017.
Lv, Z. F., Wang, X. T., Deng, F. Y., Ying, Q., Archibald, A. T., Jones, R. L., Ding, Y., Cheng, Y., Fu, M. L., Liu, Y., Man, H. Y., Xue, Z. G., He, K. B., Hao, J. M., and Liu, H. A.: Source-Receptor Relationship Revealed by the Halted Traffic and Aggravated Haze in Beijing during the COVID-19 Lockdown, Environ Sci Technol, 54, 15660-15670, 10.1021/acs.est.0c04941, 2020.
Mahowald, N., Ward, D. S., Kloster, S., Flanner, M. G., Heald, C. L., Heavens, N. G., Hess, P. G., Lamarque, J. F., and Chuang, P. Y.: Aerosol Impacts on Climate and Biogeochemistry, in: ANNUAL REVIEW OF ENVIRONMENT AND RESOURCES, VOL 36, edited by: Gadgil, A., and Liverman, D. M., 45-74, 10.1146/annurev-environ-042009-094507, 2011.
Matsui, H., Hamilton, D. S., and Mahowald, N. M.: Black carbon radiative effects highly sensitive to emitted particle size when resolving mixing-state diversity, NATURE COMMUNICATIONS, 9, 10.1038/s41467-018-05635-1, 2018.
Meng, Y., Zhou, J., Wang, Z., Tang, W., Ma, J., Zhang, T., and Long, Z.: Retrieval of nighttime aerosol optical depth by simultaneous consideration of artificial and natural light sources, SCIENCE OF THE TOTAL ENVIRONMENT, 896, 10.1016/j.scitotenv.2023.166354, 2023.
Mitra, A. K., Sharma, A. K., Soni, V. K., and Kundu, P. K.: Characteristics of recent dust storms over the Indian region using real time multi-satellite observations from the direct broadcast receiving system at IMD, AdSpR, 51, 1195-1203, 10.1016/j.asr.2012.11.017, 2013.
Nembrini, S., König, I. R., and Wright, M. N.: The revival of the Gini importance?, BIOINFORMATICS, 34, 3711-3718, 10.1093/bioinformatics/bty373, 2018.
Ou, Y., Zhao, W., Wang, J., Zhao, W., and Zhang, B.: Characteristics of Aerosol Types in Beijing and the Associations with Air Pollution from 2004 to 2015, REMOTE SENSING, 9, 10.3390/rs9090898, 2017.
Panicker, A. S., Pandithurai, G., Safai, P. D., and Kewat, S.: Observations of enhanced aerosol longwave radiative forcing over an urban environment, GEOPHYSICAL RESEARCH LETTERS, 35, 10.1029/2007GL032879, 2008.
Payne, V. H., Mlawer, E. J., Cady-Pereira, K. E., and Moncet, J. L.: Water Vapor Continuum Absorption in the Microwave, IEEE TRANSACTIONS ON GEOSCIENCE AND REMOTE SENSING, 49, 2194-2208, 10.1109/TGRS.2010.2091416, 2011.
Pérez-Ramírez, D., Lyamani, H., Olmo, F. J., and Alados-Arboledas, L.: Improvements in star photometry for aerosol characterizations, JAerS, 42, 737-745, 10.1016/j.jaerosci.2011.06.010, 2011.
Pérez-Ramírez, D., Lyamani, H., Olmo, F. J., Whiteman, D. N., and Alados-Arboledas, L.: Columnar aerosol properties from sun-and-star photometry: statistical comparisons and day-to-night dynamic, ATMOSPHERIC CHEMISTRY AND PHYSICS, 12, 9719-9738, 10.5194/acp-12-9719-2012, 2012.
Pérez-Ramírez, D., Ruiz, B., Aceituno, J., Olmo, F. J., and Alados-Arboledas, L.: Application of Sun/star photometry to derive the aerosol optical depth, IJRS, 29, 5113-5132, 10.1080/01431160802036425, 2008.
Pérez-Ramírez, D., Lyamani, H., Smirnov, A., O'Neill, N. T., Veselovskii, I., Whiteman, D. N., Olmo, F. J., and Alados-Arboledas, L.: Statistical study of day and night hourly patterns of columnar aerosol properties using sun and star photometry, REMOTE SENSING OF CLOUDS AND THE ATMOSPHERE XXI, WOS:000391488200014, 10.1117/12.2242372, 2016.

删除[gyliu]: Mhawish, A., Banerjee, T., Broday, D. M., Misra, A., and Tripathi, S. N.: Evaluation of MODIS Collection 6 aerosol retrieval algorithms over Indo-Gangetic Plain: Implications of aerosols types and mass loading, REMOTE SENSING OF ENVIRONMENT, 201, 297-313, 10.1016/j.rse.2017.09.016, 2017.

删除[gyliu]: Omar, A. H., Winker, D. M., Tackett, J. L., Giles, D. M., Kar, J., Liu, Z., Vaughan, M. A., Powell, K. A., and Trepte, C. R.: CALIOP and AERONET aerosol optical depth comparisons: One size fits none, JOURNAL OF GEOPHYSICAL RESEARCH-ATMOSPHERES, 118, 4748-4766, 10.1002/jgrd.50330, 2013.

Pérez-Ramírez, D., Veselovskii, I., Whiteman, D. N., Suvorina, A., Korenskiy, M., Kolgotin, A., Holben, B., Dubovik, O., Siniuk, A., and Alados-Arboledas, L.: High temporal resolution estimates of columnar aerosol microphysical parameters from spectrum of aerosol optical depth by linear estimation: application to long-term AERONET and star-photometry measurements, ATMOSPHERIC MEASUREMENT TECHNIQUES, 8, 3117-3133, 10.5194/amt-8-3117-2015, 2015.

Perrone, M. R., Lorusso, A., and Romano, S.: Diurnal and nocturnal aerosol properties by AERONET sun-sky-lunar photometer measurements along four years, ATMOSPHERIC RESEARCH, 265, 10.1016/j.atmosres.2021.105889, 2022.

Pierangelo, C., Mishchenko, M., Balkanski, Y., and Chédin, A.: Retrieving the effective radius of Saharan dust coarse mode from AIRS -: art. no. L20813, GEOPHYSICAL RESEARCH LETTERS, 32, 10.1029/2005GL023425, 2005.

Pierangelo, C., Chédin, A., Heilliette, S., Jacquinet-Husson, N., and Armante, R.: Dust altitude and infrared optical depth from AIRS, ATMOSPHERIC CHEMISTRY AND PHYSICS, 4, 1813-1822, 10.5194/acp-4-1813-2004, 2004.

Quan, J. N., Jiang, C. L., Xin, J. Y., Zhao, X. J., Jia, X. C., Liu, Q., Gao, Y., and Chen, D.: Evaluation of satellite aerosol retrievals with in situ aircraft and ground measurements: Contribution of relative humidity, ATMOSPHERIC RESEARCH, 212, 1-5, 10.1016/j.atmosres.2018.04.024, 2018.

Riemer, N., Ault, A. P., West, M., Craig, R. L., and Curtis, J. H.: Aerosol Mixing State: Measurements, Modeling, and Impacts, REVIEWS OF GEOPHYSICS, 57, 187-249, 10.1029/2018RG000615, 2019.

Rogers, R. R., Vaughan, M. A., Hostetler, C. A., Burton, S. P., Ferrare, R. A., Young, S. A., Hair, J. W., Obland, M. D., Harper, D. B., Cook, A. L., and Winker, D. M.: Looking through the haze: evaluating the CALIPSO level 2 aerosol optical depth using airborne high spectral resolution lidar data, ATMOSPHERIC MEASUREMENT TECHNIQUES, 7, 4317-4340, 10.5194/amt-7-4317-2014, 2014.

Santa Maria, M. and Winker, D.: Sampling uncertainties in observing the global aerosol with a nadir-viewing satellite lidar, LIDAR REMOTE SENSING FOR INDUSTRY AND ENVIRONMENTAL MONITORING V, WOS:000227658800037, 10.1117/12.583098, 2005.

Sayer, A. M., Hsu, N. C., Lee, J., Kim, W. V., and Dutcher, S. T.: Validation, Stability, and Consistency of MODIS Collection 6.1 and VIIRS Version 1 Deep Blue Aerosol Data Over Land, JOURNAL OF GEOPHYSICAL RESEARCH-ATMOSPHERES, 124, 4658-4688, 10.1029/2018JD029598, 2019.

Seinfeld, J. H., Bretherton, C., Carslaw, K. S., Coe, H., DeMott, P. J., Dunlea, E. J., Feingold, G., Ghan, S., Guenther, A. B., Kahn, R., Kraucunas, I., Kreidenweis, S. M., Molina, M. J., Nenes, A., Penner, J. E., Prather, K. A., Ramanathan, V., Ramaswamy, V., Rasch, P. J., Ravishankara, A. R., Rosenfeld, D., Stephens, G., and Wood, R.: Improving our fundamental understanding of the role of aerosol-cloud interactions in the climate system, PROCEEDINGS OF THE NATIONAL ACADEMY OF SCIENCES OF THE UNITED STATES OF AMERICA, 113, 5781-5790, 10.1073/pnas.1514043113, 2016.

Song, Q. Q., Zhang, Z. B., Yu, H. B., Kok, J. F., Di Biagio, C., Albani, S., Zheng, J. Y., and Ding, J. C.: Size-resolved dust direct radiative effect efficiency derived from satellite observations, ATMOSPHERIC CHEMISTRY AND PHYSICS, 22, 13115-13135, 10.5194/acp-22-13115-2022, 2022.

Stenchikov, G., Robock, A., Ramaswamy, V., Schwarzkopf, M. D., Hamilton, K., and Ramachandran, S.: Arctic Oscillation response to the 1991 Mount Pinatubo eruption: Effects of volcanic aerosols and

删除[gyliu]: Sinyuk, A., Holben, B. N., Eck, T. F., Giles, D. M., Slutsker, I., Korkin, S., Schafer, J. S., Smirnov, A., Sorokin, M., and Lyapustin, A.: The AERONET Version 3 aerosol retrieval algorithm, associated uncertainties and comparisons to Version 2, ATMOSPHERIC MEASUREMENT TECHNIQUES, 13, 3375-3411, 10.5194/amt-13-3375-2020, 2020.

ozone depletion, JOURNAL OF GEOPHYSICAL RESEARCH-ATMOSPHERES, 107, 10.1029/2002JD002090, 2002.
Su, X., Huang, Y. H., Wang, L. C., Cao, M. D., and Feng, L.: Validation and diurnal variation evaluation of MERRA-2 multiple aerosol properties on a global scale, ATMOSPHERIC ENVIRONMENT, 311, 10.1016/j.atmosenv.2023.120019, 2023.
Sulaymon, I. D., Zhang, Y. X., Hopke, P. K., Hu, J. L., Zhang, Y., Li, L., Mei, X. D., Gong, K. J., Shi, Z. H., Zhao, B., and Zhao, F. X.: Persistent high PM2.5 pollution driven by unfavorable meteorological conditions during the COVID-19 lockdown period in the Beijing-Tianjin-Hebei region, China, Environ Res, 198, 10.1016/j.envres.2021.111186, 2021.
Sun, J. Y. T., Veefkind, P., van Velthoven, P., and Levelt, P. F.: Aerosol Absorption Over Land Derived From the Ultra-Violet Aerosol Index by Deep Learning, IEEE JOURNAL OF SELECTED TOPICS IN APPLIED EARTH OBSERVATIONS AND REMOTE SENSING, 14, 9692-9710, 10.1109/JSTARS.2021.3108669, 2021.
Svetnik, V., Liaw, A., Tong, C., Culberson, J. C., Sheridan, R. P., and Feuston, B. P.: Random forest: A classification and regression tool for compound classification and QSAR modeling, J Chem Inf Comput Sci, 43, 1947-1958, 10.1021/ci034160g, 2003.
Tao, C. L., Wheiler, K., Yu, C., Cheng, B. D., and Diao, G.: Does the joint prevention and control regulation improve the air quality? A quasi-experiment in the Beijing economic belt during the COVID-19 pandemic, SUSTAINABLE CITIES AND SOCIETY, 75, 10.1016/j.scs.2021.103365, 2021.
Tindan, J. Z., Jin, Q. J., and Pu, B.: Understanding day-night differences in dust aerosols over the dust belt of North Africa, the Middle East, and Asia, ATMOSPHERIC CHEMISTRY AND PHYSICS, 23, 5435-5466, 10.5194/acp-23-5435-2023, 2023.
Van Leeuwen, G. M. J., Hand, J. W., de Kamer, J. B., and Mizushina, S.: Temperature retrieval algorithm for brain temperature monitoring using microwave brightness temperatures, ELECTRONICS LETTERS, 37, 341-342, 10.1049/el:20010269, 2001.
Varga, A. J. and Breuer, H.: Evaluation of convective parameters derived from pressure level and native ERA5 data and different resolution WRF climate simulations over Central Europe, CLIMATE DYNAMICS, 58, 1569-1585, 10.1007/s00382-021-05979-3, 2022.
Visioni, D., Bednarz, E. M., Lee, W. R., Kravitz, B., Jones, A., Haywood, J. M., and MacMartin, D. G.: Climate response to off-equatorial stratospheric sulfur injections in three Earth system models - Part 1: Experimental protocols and surface changes, ATMOSPHERIC CHEMISTRY AND PHYSICS, 23, 663-685, 10.5194/acp-23-663-2023, 2023.
Wang, H. Z., Zhang, R., Wang, G. H., An, Y. Z., and Jin, B. G.: Quality control of Argo temperature and salinity observation profiles, CHINESE JOURNAL OF GEOPHYSICS-CHINESE EDITION, 55, 577-588, 10.6038/j.issn.0001-5733.2012.02.020, 2012.
Wang, J., Xia, X. G., Wang, P. C., and Christopher, S. A.: Diurnal variability of dust aerosol optical thickness and Angstrom exponent over dust source regions in China, GEOPHYSICAL RESEARCH LETTERS, 31, 10.1029/2004GL019580, 2004.
Wang, L. T., Wei, Z., Yang, J., Zhang, Y., Zhang, F. F., Su, J., Meng, C. C., and Zhang, Q.: The 2013 severe haze over southern Hebei, China: model evaluation, source apportionment, and policy implications, ATMOSPHERIC CHEMISTRY AND PHYSICS, 14, 3151-3173, 10.5194/acp-14-3151-2014, 2014.

Wang, N., Hu, Y., Li, X. M., Kang, C., and Yan, L.: AOD Derivation from SDGSAT-1/GLI Dataset in Mega-City Area, REMOTE SENSING, 15, 10.3390/rs15051343, 2023.
Wang, S. Y., Li, F. X., de Leeuw, G., Fan, C., and Li, Z. Q.: A multilevel downscaling model for enhancing nocturnal aerosol optical depth reanalysis from CAMS over the Beijing-Tianjin-Hebei region, China, ENVIRONMENTAL TECHNOLOGY & INNOVATION, 39, 10.1016/j.eti.2025.104238, 2025.
Wang, X., Mu, X., and Yan, G.: Quantitative Analysis of Aerosol Influence on Suomi-NPP VIIRS Nighttime Light in China, IEEE JOURNAL OF SELECTED TOPICS IN APPLIED EARTH OBSERVATIONS AND REMOTE SENSING, 13, 3557-3568, 10.1109/JSTARS.2020.3003480, 2020.
Wei, L. Y., Wang, Y., Liu, S., Zhang, G., and Wang, B.: Distinct roles of land cover in regulating spatial variabilities of temperature responses to radiative effects of aerosols and clouds, ENVIRONMENTAL RESEARCH LETTERS, 16, 10.1088/1748-9326/ac3f04, 2021.
Xie, Y., Chen, J. X., Liu, D. W., Lv, C. C., Liu, K., and Miao, J. G.: DEVELOPMENT AND CALIBRATION OF A K-BAND GROUND-BASED HYPERSPECTRAL MICROWAVE RADIOMETER FOR WATER VAPOR MEASUREMENTS, PROGRESS IN ELECTROMAGNETICS RESEARCH-PIER, 140, 415-438, 10.2528/PIER13050704, 2013.
Yang, Z. M., Zdanski, C., Farkas, D., Bang, J., and Williams, H.: Evaluation of Aerosol Optical Depth (AOD) and PM_{2.5} associations for air quality assessment, REMOTE SENSING APPLICATIONS-SOCIETY AND ENVIRONMENT, 20, 10.1016/j.rsase.2020.100396, 2020.
Yu, X. N., Zhu, B., and Zhang, M. G.: Seasonal variability of aerosol optical properties over Beijing, ATMOSPHERIC ENVIRONMENT, 43, 4095-4101, 10.1016/j.atmosenv.2009.03.061, 2009.
Yu, Y., Kalashnikova, O. V., Garay, M. J., Lee, H., Choi, M., Okin, G. S., Yorks, J. E., Campbell, J. R., and Marquis, J.: A global analysis of diurnal variability in dust and dust mixture using CATS observations, ATMOSPHERIC CHEMISTRY AND PHYSICS, 21, 1427-1447, 10.5194/acp-21-1427-2021, 2021.
Zhang, J., Jaker, S. L., Reid, J. S., Miller, S. D., Solbrig, J., and Toth, T. D.: Characterization and application of artificial light sources for nighttime aerosol optical depth retrievals using the Visible Infrared Imager Radiometer Suite Day/Night Band, ATMOSPHERIC MEASUREMENT TECHNIQUES, 12, 3209-3222, 10.5194/amt-12-3209-2019, 2019.
Zhang, L., Liu, M., He, W., Xia, X., Yu, H., Li, S., and Li, J.: Ground Passive Microwave Remote Sensing of Atmospheric Profiles Using WRF Simulations and Machine Learning Techniques, Journal of Meteorological Research, 38, 680-692, 10.1007/s13351-024-4004-2, 2024.
Zhang, L. L., Liu, M. J., He, W. Y., Xia, X. A.,Yu, H. N., Li, S. X., Li, J.: Ground Passive Microwave Remote Sensing of Atmospheric Profiles Using WRF Simulations and Machine Learning Techniques, Journal of Meteorological Research, 10.1007/s13351-024-4004-2, 2024.
Zhang, X. Y., Xu, X. Y., Chen, H. S., Hu, X. M., and Gao, L.: Dust-planetary boundary layer interactions amplified by entrainment and advections, ATMOSPHERIC RESEARCH, 278, 10.1016/j.atmosres.2022.106359, 2022.
Zheng, J. Y., Zhang, Z. B., Garnier, A., Yu, H. B., Song, Q. Q., Wang, C. X., Dubuisson, P., and Di Biagio, C.: The thermal infrared optical depth of mineral dust retrieved from integrated CALIOP and IIR observations, REMOTE SENSING OF ENVIRONMENT, 270, 10.1016/j.rse.2021.112841, 2022.
Zheng, J. Y., Zhang, Z. B., Yu, H. B., Garnier, A., Song, Q. Q., Wang, C. X., Di Biagio, C., Kok, J. F., Derimian, Y., and Ryder, C.: Thermal infrared dust optical depth and coarse-mode effective diameter

over oceans retrieved from collocated MODIS and CALIOP observations, ATMOSPHERIC CHEMISTRY AND PHYSICS, 23, 8271-8304, 10.5194/acp-23-8271-2023, 2023.

Zhou, L. a., Wang, C., Miao, S., and Li, J.: Impact of the Complex Terrain in Beijing on Formation of Low-Level Jets, JOURNAL OF METEOROLOGICAL RESEARCH, 38, 138-150, 10.1007/s13351-024-3122-1, 2024.

Zhou, M., Wang, J., Chen, X., Xu, X., Colarco, P. R., Miller, S. D., Reid, J. S., Kondragunta, S., Giles, D. M., and Holben, B.: Nighttime smoke aerosol optical depth over US rural areas: First retrieval from VIIRS moonlight observations, REMOTE SENSING OF ENVIRONMENT, 267, 10.1016/j.rse.2021.112717, 2021.